

Inflaton Self Resonance, Oscillons, and Gravitational Waves in Small Field Polynomial Inflation

Manuel Drees* and Chenhuan Wang†

Bethe Center for Theoretical Physics and Physikalisches Institut, Universität
Bonn,
Nussallee 12, 53115 Bonn, Germany

January 24, 2025

Abstract

In this work, we investigate the post-inflationary dynamics of a simple single-field model with a renormalizable inflaton potential featuring a near-inflection point at a field value ϕ_0 . Due to the concave shape of the scalar potential, the effective mass of the inflaton becomes imaginary during as well as for some period after slow-roll inflation. As a result, in the initial reheating phase, where the inflaton oscillates around its minimum with a large amplitude, some field fluctuations grow exponentially; this effect becomes stronger at smaller ϕ_0 . This aspect can be analyzed using the Floquet theorem. We also analytically estimate the back reaction time after which the perturbations affect the evolution of the average inflaton field. In order to fully analyze this non-perturbative regime, we perform a (classical) lattice simulation, which reveals that the exponential growth of field fluctuations can fragment the system. This leads to a large amount of non-Gaussianity at very small scales, but the equation of state remains close to matter-like. The evolution of the background field throughout the fragmentation phase can be understood using the Hartree approximation. For sufficiently small ϕ_0 soliton-like objects, called oscillons in the literature, are formed. This leads to areas with high local over-density, $\delta\rho \gg \bar{\rho}$ where $\bar{\rho}$ is the average energy density. We speculate that this could lead to the formation of light primordial black holes, with lifetime $\gtrsim 10^{-19}$ sec. Other possibly observational consequences, in particular gravitational waves in the MHz – GHz range, are discussed as well. Although a complete analytical study is difficult in our case, we obtain a power law scaling for the potential observables on ϕ_0 .

1 Introduction

Inflation as a theory of the very early Universe predicts the origin of density perturbations and their *coherent* phases after they re-enter the horizon [1, 2]. The simplest realization, using a single inflaton field undergoing slow-roll, remains compatible with all observations [3] as long as the scalar potential $V(\phi)$ is sufficiently flat. Moreover, if inflation occurs for field values well below the Planck

*drees@th.physik.uni-bonn.de

†cwang1@uni-bonn.de

scale, a spectral index of density perturbations below 1, as indicated by observation, can only be realized if the second derivative of the potential is negative during inflation, leading to a *tachyonic* inflaton mass. In many cases this tachyonic mass will persist at the onset of reheating, when the inflaton field begins to oscillate around its minimum.

It has been realized some time ago that there are non-perturbative channels for the inflaton to transfer its energy to other fields, see e.g. [4–7]. Here we investigate the closely related tachyonic resonance, which occurs due to the inflaton self-couplings. We perform our analysis for a particularly simple model [8], which assumes a renormalizable potential featuring a near-inflection point at a field value ϕ_0 , with inflation occurring at ϕ just below ϕ_0 . We find that the tachyonic resonance can lead to ample “particle production”, i.e. the production of modes of the inflaton field with finite momentum.

In the model we consider, a tachyonic inflaton mass at large field values implies that the potential is shallower than quadratic near the minimum for $\phi > 0$. It is known that a shallower than quadratic potential can lead [9] to the formation of soliton-like objects, called *oscillons*. We show that such objects are also generated in our model, even though the potential is steeper than quadratic for $\phi < 0$, i.e. for “half” of each oscillation of the inflaton field. These *oscillons* are relatively long-lived and highly localized. As a result, primordial black holes (PBHs) might be produced [10–12]. Moreover, during their formation the *oscillons* emit high frequency gravitational waves (GWs) [11, 13–18]. (See also the review [19].)

The remainder of this article is organized as follows. In section 2, the model we consider is briefly introduced and a first hint for a self-resonance is presented. In section 3, we use the Floquet theorem in order to check the amount and range of instability. For the final, credible result we use lattice simulations; they are discussed in section 4. Possible observational consequences are analyzed in section 5. Finally, the results will be summarized in section 6.

In this work, we use the reduced Planck mass $m_{\text{Pl}} = 2.44 \times 10^{18}$ GeV. Derivatives with respect to the cosmic time t are denoted with a dot, e.g. $\dot{\phi} = \partial\phi/\partial t$. The derivative of the scalar potential is defined as

$$V'(\phi) = V_{,\phi}(\phi) = \partial_{\phi}V(\phi). \quad (1.1)$$

Similarly, V'' denotes the second derivative of $V(\phi)$. Except where explicitly noted, k refers to the comoving momentum or wave vector, i.e. $k = qa$ with q the physical momentum and a the (dimensionless) scale factor; the latter is normalized such that $a = 1$ at the end of inflation. The following tools and programs are used in this project: SciPy 1.0 [20], NumPy [21], Scikit-learn [22], Matplotlib [23], PyVista [24], HDF5 [25], CosmoLattice [26], and HLATTICE [13].

2 Inflationary model

Our analysis is based on the model proposed in [8]. It is the unique single-field model with a purely renormalizable potential that agrees with observations. The inflaton potential is given by

$$V(\phi) = d \left[\phi^2 - \frac{8}{3}(1 - \beta)\phi_0\phi + 2\phi_0^2 \right] \phi^2. \quad (2.1)$$

The observational upper bound on primordial tensor modes implies $\phi_0 < 22 m_{\text{Pl}}$ [27]. However, we will see shortly that interesting nonlinear dynamics occurs in the post-inflationary epoch only in the small-field version of the model, where ϕ_0 is well below m_{Pl} . In this model, density perturbations observed in the CMB were generated at field values just below ϕ_0 . By fitting the Planck 2018 data [28], in particular the central values of the scalar power spectrum amplitude A_s and of the scalar

spectral index n_s , and requiring $N_{\text{CMB}} = 65$ e-folds of inflation after the CMB pivot scale first crossed out of the horizon, the model parameters are determined to be

$$\beta = 9.73 \times 10^{-7} \left(\frac{\phi_0}{m_{\text{Pl}}} \right)^4, \quad d = 6.61 \times 10^{-16} \left(\frac{\phi_0}{m_{\text{Pl}}} \right)^2; \quad (2.2)$$

these numbers depend only weakly on N_{CMB} [8]. Thus, ϕ_0 is essentially the only free parameter left.

In order to recover the hot big bang, a reheating phase must be invoked. To that end one can introduce a Yukawa coupling to fermions and/or a cubic coupling $\phi|\phi'|^2$ to complex scalar fields ϕ' . In order to preserve the flatness of the potential necessary for slow-roll inflation, one should require that the (1-loop) radiative corrections due to these new couplings to the derivatives of the inflaton potential don't exceed the tree level contributions. In combination with the lower bound on the reheat temperature for successful big bang nucleosynthesis, this leads to a lower bound on ϕ_0 , $\phi_0 > 3.40 \times 10^{-5} m_{\text{Pl}}$ [8].

At least within the usual cosmological models, the Planck data require the spectral index of the density perturbations to be smaller than 1 [28] at

$$n_s = 0.9659 \pm 0.0040. \quad (2.3)$$

In slow-roll inflation, n_s is predicted to be [29]

$$n_s = 1 - 6\epsilon_V + 2\eta_V, \quad (2.4)$$

where the (potential) slow-roll parameters are given by

$$\epsilon_V = \frac{m_{\text{Pl}}^2}{2} \left(\frac{V'}{V} \right)^2; \quad \eta_V = m_{\text{Pl}}^2 \frac{V''}{V}. \quad (2.5)$$

In small-field inflation, one has generically $\epsilon_V \ll |\eta_V|$; this is true also in our model. A spectral index below unity can then only be realized if the potential is concave, i.e. has a negative second derivative, leading to a negative (field-dependent) squared mass of the inflaton. In our model, the latter is given by¹

$$\tilde{m}^2(\phi) = V''(\phi) = 12d \left[\left(\phi - \frac{2}{3}\phi_0 \right)^2 - \frac{1}{9}\phi_0^2 \right]. \quad (2.6)$$

Thus, the inflaton will become tachyonic if the field lies in the range

$$\phi_0/3 < \phi < \phi_0, \quad (2.7)$$

but has a positive squared mass elsewhere. The minimum value of the squared mass is

$$-|\tilde{m}_{\text{min}}|^2 = \min(\tilde{m}^2) = -\frac{4}{3}d\phi_0^2 = -\frac{1}{3}m_\phi^2, \quad (2.8)$$

where

$$m_\phi = 2\sqrt{d}\phi_0 \quad (2.9)$$

is the inflaton rest mass after the end of inflation (including now). m_ϕ also sets the timescale for inflaton oscillations even for large amplitude oscillations where the anharmonicity is sizable, and will therefore be a convenient unit later on.

¹We're neglecting the small contribution $\propto \beta$, which is relevant during inflation but not afterwards.

A tachyonic instability can only occur if the inflaton field is in the range (2.7). As a first step we show that, in the absence of backreaction effects, the time the Universe spends in this tachyonic regime increases with decreasing ϕ_0 . The equation of motion for the background field, assumed to be spatially constant, is:

$$\ddot{\phi} + 3H\dot{\phi} + V'(\phi) = 0. \quad (2.10)$$

Here $H = \dot{a}/a$ is the Hubble parameter. It is given by

$$H^2 = \frac{\rho_K + \rho_V}{3m_{\text{Pl}}^2}, \quad (2.11)$$

where the energy components are

$$\rho_K = \frac{1}{2} (\dot{\phi})^2, \quad \rho_V = V(\phi). \quad (2.12)$$

During inflation, ρ_K is negligible and $H \simeq H_I = \sqrt{d\phi_0^2/(3m_{\text{Pl}})}$ is essentially constant; after inflation, $H < H_I$ decreases. The crucial observation is that $m_\phi/H_I = 6m_{\text{Pl}}/\phi_0$, i.e. the relative importance of the damping term in eq.(2.10) decreases $\propto 1/\phi_0$.

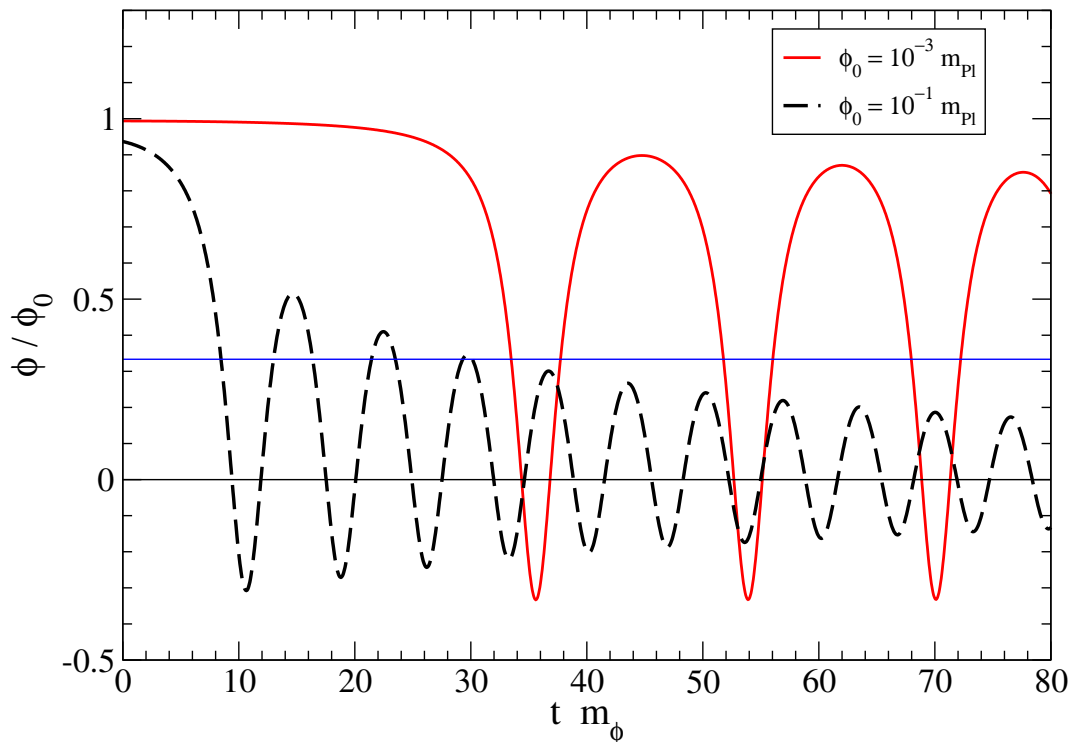


Figure 1: Evolution of the (spatially constant) background inflaton field according to eqs.(2.10) and (2.11), for $\phi_0 = 0.1 m_{\text{Pl}}$ (dashed black) and $\phi_0 = 10^{-3} m_{\text{Pl}}$ (solid red). The inflaton field is given in units of ϕ_0 , and the time in units of $1/m_\phi$, with $t = 0$ denoting the time when $\epsilon_V = 0.1$. The inflaton is tachyonic if the field is above the thin blue line.

This is illustrated in fig. 1, which shows the evolution of the classical inflaton field after the end of slow-roll inflation; the latter is (somewhat arbitrarily) defined by² $\epsilon_V = 0.1$, which implies $\phi = \phi_0 (1 - 0.2\sqrt{\phi_0/m_{\text{Pl}}})$. For $\phi_0 = 0.1 m_{\text{Pl}}$ (black dashed curve) the field quickly starts to oscillate. Because damping is sizable, it re-enters the tachyonic regime only three times; by $t m_\phi = 80$ the oscillations have become quite harmonic. In contrast, for $\phi_0 = 10^{-3} m_{\text{Pl}}$ (solid red curve), field oscillations only start at $t \simeq 30/m_\phi$. Since damping is much less important, the oscillations remain very anharmonic even at $t = 80/m_\phi$, with the inflaton field spending most of its time in the tachyonic range (2.7). In fact, our numerical analysis shows that, if the dynamics was entirely determined by eqs.(2.10) and (2.11), the number of times the inflaton field re-enters the tachyonic regime would simply scale $\propto 1/\phi_0$.

The evolution of the background field is of interest mainly because it may allow some perturbations to grow exponentially. This tachyonic instability comes about if for some wave vectors \vec{k} the inflaton perturbation $\delta\phi_{\vec{k}}$ develops an imaginary frequency ω_k . To linear order, $\delta\phi_{\vec{k}}$ satisfies the equation of motion

$$\delta\ddot{\phi}_{\vec{k}} + 3H\delta\dot{\phi}_{\vec{k}} + \omega_k^2(t)\delta\phi_{\vec{k}} = 0, \quad \text{with} \quad \omega_k^2 = k^2/a^2 + \tilde{m}^2(\phi). \quad (2.13)$$

We see that $\omega_k^2 < 0$ when the background field ϕ lies in the range (2.7) and $k^2 \equiv \vec{k}^2 < -a^2\tilde{m}^2(\phi)$.

During inflation, \tilde{m}^2 is negative but small in magnitude: $|\eta_V| \ll 1$ implies $|\tilde{m}^2| \ll H^2$. The tachyonic instability therefore has negligible effect during the slow-roll epoch.

In contrast, during the oscillatory phase, i.e. in the reheating epoch, $m_\phi^2 > H^2$. Setting $H = 0$ to zeroth-order approximation, the solution of eq.(2.13) can approximately be written as [30, 31]

$$\delta\phi_{\vec{k}} = \frac{A_{\vec{k}}}{\sqrt{2\omega_k(t)}} \exp\left[-i \int^t \omega_k(t') dt'\right] + \frac{B_{\vec{k}}}{\sqrt{2\omega_k(t)}} \exp\left[+i \int^t \omega_k(t') dt'\right], \quad (2.14)$$

where the coefficients $A_{\vec{k}}$ and $B_{\vec{k}}$ are determined by the initial conditions. This approximation is only valid when the frequency $\omega_k(t)$ is changing slowly (or adiabatically), $|\dot{\omega}|/\omega^2 \ll 1$. For $\omega_k^2 < 0$, the solution (2.14) evidently has exponentially decaying and exponentially growing solutions; clearly the latter will dominate at late times.

As already noted, the approximate solution (2.14) has been derived by setting $H = 0$ in the equation of motion. This is reasonable only for modes well inside the horizon, i.e. for physical momentum $q = k/a > H$. We saw above that $m_\phi \gg H$, and hence $|\tilde{m}_{\text{min}}| \gg H$, if $\phi_0 \ll m_{\text{Pl}}$; exponential growth can then occur for $|\tilde{m}_{\text{min}}| > q > H$. Note also that for an effectively matter-dominated universe, $H \propto a^{-3/2}$ decreases faster than the physical momentum $q \propto a^{-1}$, i.e. a mode that is inside the Hubble horizon at the onset of inflaton field oscillations will remain inside the horizon.

Fig. 2 shows some numerical solutions of eq.(2.13) for $\phi_0 = 10^{-3} m_{\text{Pl}}$; the evolution of the background field has again be computed from eqs.(2.10) and (2.11). We have initialized the Fourier modes at the onset of oscillations, defined by the time when the background field first crosses zero; q is the physical momentum at that time. For simplicity we have set the initial time derivative $\delta\dot{\phi}_k$ to zero. Since eq.(2.13) is linear, the solution is then proportional to the initial value. We see that the mode with $q = m_\phi$ (dashed green curve), which is outside the tachyonic window, oscillates with an amplitude that stays roughly constant over the range of time shown; eventually it gets damped by the Hubble expansion. The mode with $q = 0.01 m_\phi$ (blue dotted curve) does have a tachyonic mass; however, since its initial wavelength is comparable to the Hubble radius, it also does not

²At this point $|\eta_V|$ is typically already well above 1. However, since the equation of motion (2.10) depends on the first derivative of the potential, and thus on $\sqrt{\epsilon_V}$ rather than on η_V , ϕ stays close to ϕ_0 until ϵ_V becomes sizable.

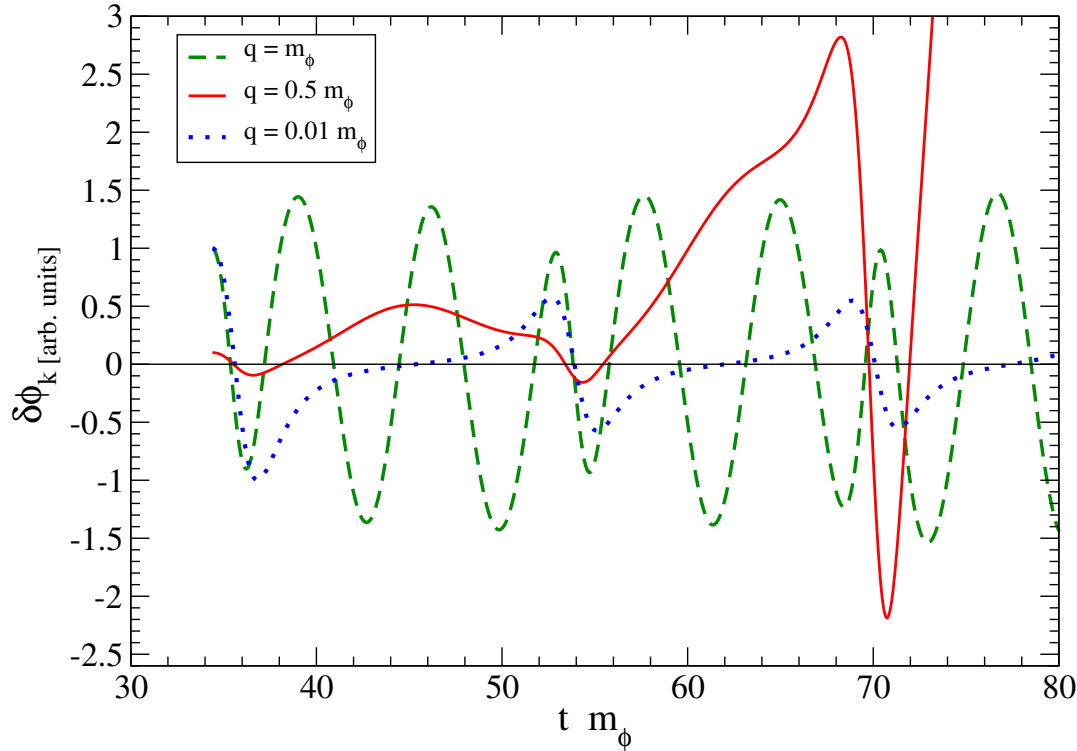


Figure 2: Evolution of some Fourier modes of the inflaton field for $\phi_0 = 10^{-3} m_{\text{Pl}}$. q is the absolute value of the physical wave vector at the time when the background field first crosses zero. At this “initial” time, the time derivative of the perturbation has been set to zero; $\delta\phi_k$ has been set to 1 for $q = m_\phi$ (dashed green) and for $q = 0.01 m_\phi$ (dotted blue), but to 0.1 for $q = 0.5 m_\phi$ (solid red). Since the evolution equation (2.13) is linear in $\delta\phi_k$, its initial value simply scales the curves up or down.

show significant growth. In contrast, the mode with $q = 0.5 m_\phi$ (solid red) grows very quickly, each maximum being about a factor of 5 above the previous one. This confirms our qualitative discussion above.

3 Floquet analysis

In this section we investigate the exponential growth of some modes more quantitatively. We stay in the linear regime where the field perturbation $\delta\phi$ is small compared to the background field $\langle\phi\rangle$. This Floquet analysis will also be helpful for setting the lattice parameters later on. Moreover, it will allow us to estimate the time when the back-reaction of the perturbation modes on the evolution of the background field becomes important; beyond this point the perturbative analysis will no longer work. Finally, we’ll present a simple analytical model which confirms our numerical results.

3.1 Linearized equation for field fluctuations

The goal is to solve equation (2.13) for given k . More exactly, we want to identify the exponentially growing modes, and estimate just how fast they grow. To this end we perform a Floquet analysis. The Floquet theorem states that for equations of motion with periodic frequency $\omega_k(t)$, the solutions have the form

$$y_k(t) = A(t)e^{\mu_k t} + B(t)e^{-\mu_k t}, \quad (3.1)$$

with $A(t)$ and $B(t)$ being periodic functions and μ_k a momentum-dependent complex number: the Floquet exponent. Evidently modes with $\Re(\mu_k) \neq 0$ will experience exponential growth; these modes might therefore ultimately affect the background field evolution [32].

For the Floquet theorem to work, there should be no damping term and the frequency $\omega_k^2(t) = k^2/a^2 + \tilde{m}^2(\phi)$ needs to be strictly periodic (in time). Thus, we have to set $H(t) \rightarrow 0$ everywhere, including in the evolution of the background field, which then becomes perfectly periodic. In our case this can be a good approximation only for $\phi_0 \ll m_{\text{Pl}}$, where the amplitude of the background field oscillation indeed decreases very slowly as we saw in fig. 1. The effective mass \tilde{m}^2 is thus computed from the numerical solution of eq.(2.10) with $H = 0$. We chose the initial conditions such that the oscillation amplitude matches the amplitude of the first “period” of the exact solution of eq.(2.10), including the damping term. This trick allows us to match more closely the real post-inflationary dynamics of our mode.

The basic idea of the Floquet analysis is to first convert the second order differential equation (2.13) into two first order differential equations, which can be written in matrix form as

$$\partial_t x(t) = U(t)x(t). \quad (3.2)$$

The solutions are encoded in a fundamental matrix $\mathcal{O}(t, t_0)$, with $\mathcal{O}(t_0, t_0)$ being the identity matrix and $x(t) = \mathcal{O}(t, t_0)x(t_0)$. By the Floquet theorem, the eigenvalues of the monodromy matrix $\mathcal{O}(t_0 + T, t_0)$ are the Floquet exponents. Here T is the period of the system; in our case $T \sim 1/m_\phi$, and the Floquet exponents depend on ϕ_0 and q . Details of computation are given in appendix A.

3.2 Numerical result

As mentioned in the previous section, the background field $\langle\phi\rangle$ is numerically calculated without the damping term. The initial amplitude is set to equal the amplitude of the first oscillation of the numerical solution of eq.(2.10) including the damping term, i.e. the value ϕ_{max} of the first maximum after the inflaton field first crossed zero. Fig. 3 shows numerical results for this quantity, as well as a convenient fit function which we use in our numerical results presented below.

Results for the Floquet exponent with the largest real part are shown in fig. 4. We see in fig. 4b that for $\phi_0 \geq 10^{-3} m_{\text{Pl}}$, smaller ϕ_0 leads to larger maximal $\Re(\mu)$, thus faster growth. This saturates for even smaller ϕ_0 , since then the loss of amplitude in the first oscillation is basically negligible, as shown in fig. 3. In fact, the Floquet analysis isn’t really applicable to $\phi_0 \gtrsim 0.1 m_{\text{Pl}}$, since then the background field re-enters the tachyonic window only a few times during oscillation, with quickly decreasing amplitude, as we saw in fig. 1; keeping this amplitude fixed, as we do here, is then a bad approximation.

We also see that the Floquet coefficient reaches its maximum for smaller k when ϕ_0 is reduced. This allows the appearance of additional instability bands at larger k for $\phi_0 < 10^{-2} m_{\text{Pl}}$, as shown in fig. 4a.

Another important feature of the Floquet map is that $\mu_{k=0} \rightarrow 0$. Physically, this can be understood since the background field itself, which corresponds to the homogeneous part with

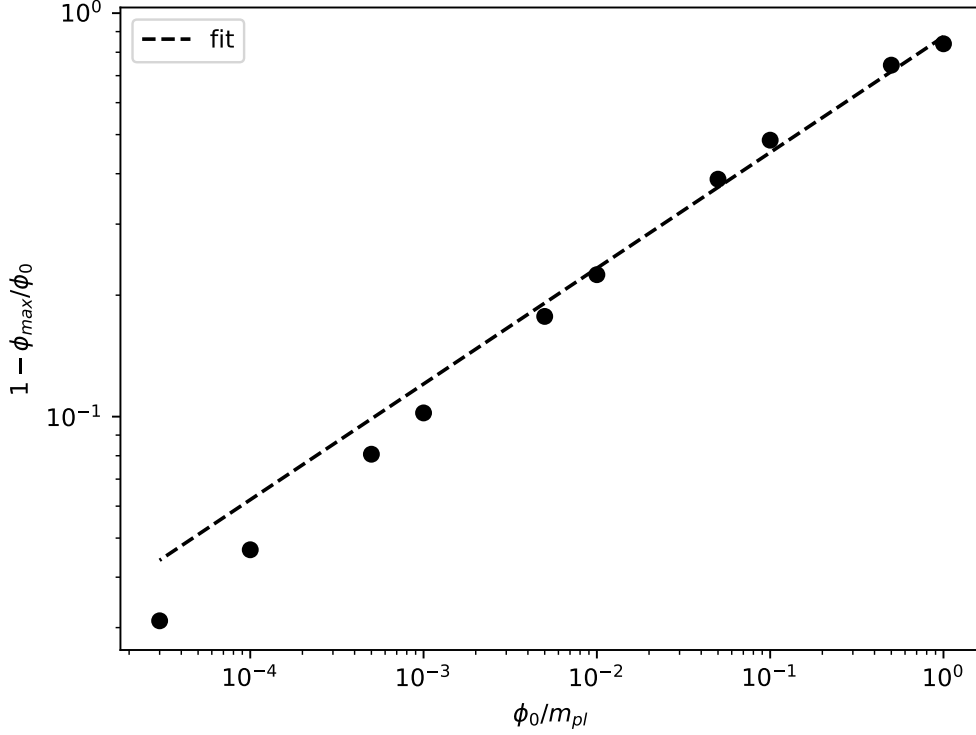


Figure 3: The “loss” of amplitude during the first oscillation in the exact equation of motion for the background field ϕ . The fit function is $1 - \phi_{\max}/\phi_0 = 0.87 \cdot (\phi/m_{\text{Pl}})^{0.29}$.

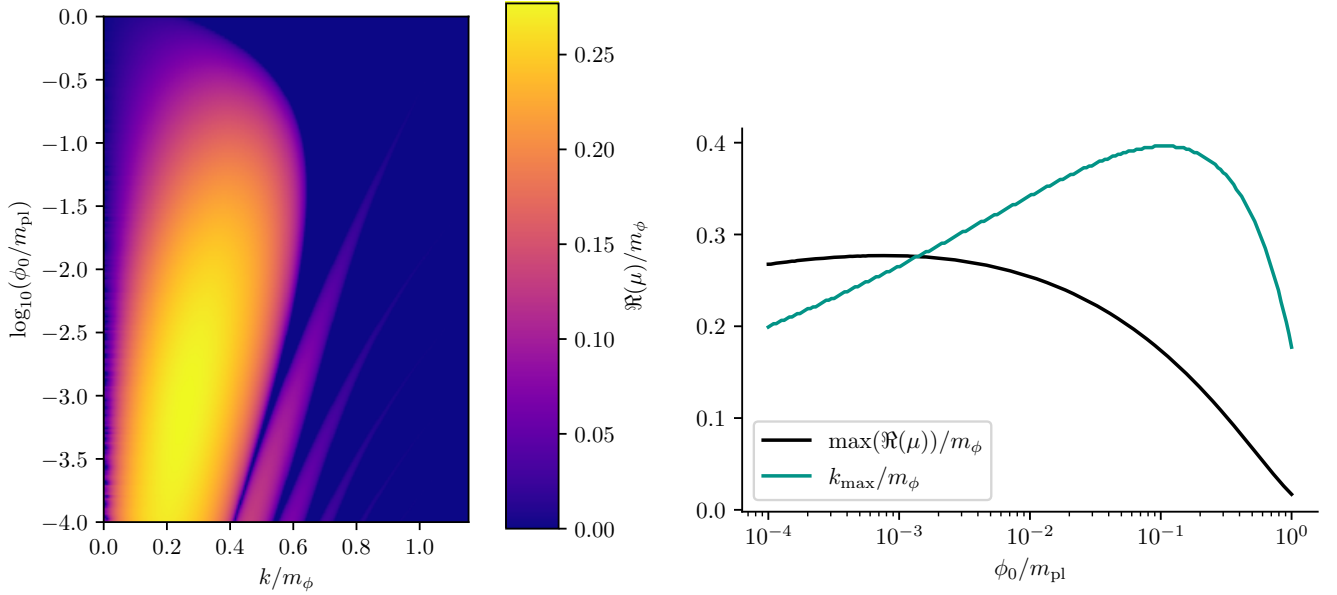
$k = 0$, should not get affected by the instability. Mathematically $k \neq 0$ is required in order to create a mismatch between the period of the perturbation and that of the background field. A nice mathematical explanation has been given in [33].

3.3 Time for back-reaction

The energy source for the growth of perturbations is the spatially homogeneous, oscillating background field, see eq.(2.13). So far we have assumed that the perturbations do not change the evolution of the background field. This is not longer true as soon as some perturbations $\delta\phi_k$ become large. Physically it is clear that the exponential growth of the perturbations cannot continue once most of the energy initially stored in the background field has been transferred to the $\delta\phi_k$.

Here we wish to estimate the time when the back-reaction becomes important. To that end we again ignore Hubble friction. We estimate the timescale of back-reaction from the maximal Floquet exponent $\Re(\mu_k)$, assuming it to be constant throughout and ignoring that the physical momenta can pass through the instability band(s). This will tend to over-estimate the growth of perturbations compared to a full numerical analysis, and thus to under-estimate the time when back-reactions become important.

This time scale depends not only on the growth rate of perturbations, but also on their size at the end of inflation (more precisely, at the time when the background field begins to oscillate around the minimum). As shown in [34, 35] one can use the standard Bunch–Davis vacuum to fix the initial condition for the fluctuations, at least for quickly growing modes where the occupation number will become large, a posteriori justifying a (semi-)classical treatment. The time scale Δt_{br}



(a) Floquet coefficients. The frequency $\omega(t)^2$ in equation (2.13) can be negative for modes with $k < m_\phi/\sqrt{3} \approx 0.58m_\phi$; note that $H = 0$ implies that $k = q$, i.e. there is no difference between co-moving and physical momenta in this approximation.

(b) Location and height of $\max(\Re(\mu))$.

Figure 4: Numerical results of Floquet analysis.

for back-reactions can thus be estimated from

$$\frac{k}{2\pi} \exp(\Re(\mu_k)\Delta t_{\text{br}}) \stackrel{!}{\simeq} \phi_0, \quad (3.3)$$

for $k = k_{\text{max}}$ where $\Re(\mu_k)$ has its maximum. This implies

$$\Delta t_{\text{br}} \simeq \frac{1}{\Re(\mu_k)} \ln \left(\frac{2\pi\phi_0}{m_\phi} \frac{m_\phi}{k_{\text{max}}} \right) = \frac{1}{\Re(\mu_k)} \left[18.6 + \ln(10) \log_{10} \left(\frac{m_{\text{Pl}}}{\phi_0} \right) - \ln \left(\frac{k_{\text{max}}}{m_\phi} \right) \right]. \quad (3.4)$$

In the second step we have used eqs.(2.9) and (2.2). Using results from the right frame of fig. 4, we see that for $\phi_0 \lesssim 0.1m_{\text{Pl}}$ it takes (at least) roughly $100 m_\phi^{-1}$ for back-reactions to become important. However, recall from fig. 1 that for $\phi_0 = 0.1m_{\text{Pl}}$ the background field no longer reaches the instability band at $t = 100 m_\phi^{-1}$, once Hubble friction is included. We thus conclude that non-linear effects in the evolution of the inflaton field will become important only for $\phi_0 < 0.1m_{\text{Pl}}$.

Recall that our Floquet analysis ignores the Hubble expansion. The reduction of the amplitude of the oscillations of the background field should be essentially irrelevant if $\Re(\mu_k) \gg H$. Since

$$\frac{\Re(\mu_k)}{H} \gtrsim \frac{\Re(\mu_k)/m_\phi}{H_I/m_\phi} = 6 \frac{\Re(\mu_k)}{m_\phi} \left(\frac{\phi_0}{m_{\text{Pl}}} \right)^{-1}, \quad (3.5)$$

this condition is satisfied for momenta near the maximum of the instability band, where $\Re(\mu_k) \geq 0.2m_\phi$, as long as $\phi_0 < 0.1m_{\text{Pl}}$. Similarly, the redshift changes physical momenta significantly only after about a Hubble time. The approximation of constant q should thus hold over the relevant period of time if $H < m_\phi/100$, which is true for $\phi_0 < 0.05 m_{\text{Pl}}$. In this range of ϕ_0 we therefore expect non-linear dynamics to become important quickly, in practice after $\mathcal{O}(10)$ oscillations of the background field.

3.4 Analytical treatment

Before turning to a fully numerical treatment of the nonlinear dynamics, we want to better understand some features of the Floquet map. In particular, we want to qualitatively discuss the dependence of the Floquet exponent on the model parameter ϕ_0 . The usual way to analytically compute the Floquet exponential is by treating the non-linearities as perturbations [36]. This does not work in our model since the potential is specifically engineered so that all terms are equally important for inflaton field values leading to a negative effective inflaton mass.

Instead we fit $\tilde{m}^2(\phi)$ in eq.(2.13) directly as a sum of delta functions and (possibly) step functions [37]. Then one can use continuity conditions in order to calculate the Floquet exponent. Our ansatz reads:

$$\omega_k^2 = -\Gamma_k^2 + \sum_{j \in \mathbb{Z}} f(t - jT) = k^2 - \Gamma_0^2 + \sum_{j \in \mathbb{Z}} f(t - jT), \quad (3.6)$$

where T is the period of the oscillation of the background field. For the “delta model”, the function $f(t)$ is simply

$$f(t) = \Lambda \delta(t), \quad (3.7)$$

while for the “box model” we assume

$$f(t) = (\tilde{\omega}_0^2 - \Gamma_0^2) \theta(T_1/2 - |t|) - \tilde{\Lambda} \delta(|t| - T_1/2). \quad (3.8)$$

The coefficients Λ and $\tilde{\Lambda}$ will be fixed through the consistency condition $\mu_{k=0} \rightarrow 0$, which is required in order to obtain the correct shape of the Floquet map. Γ_0^2 is a constant negative squared mass term; it is determined by taking the average of leftmost and rightmost points of one single period of $\tilde{m}^2(t)$. In the box model, the length (T_1) and height ($\tilde{\omega}_0^2$) of the box are determined by a least square fit.³ In turn, during the (possibly) tachyonic phase $\omega_k^2 = -\Gamma_k^2$ as in the delta model; evidently $\omega_k^2 < 0$ for $k^2 < \Gamma_0^2$. During the non-tachyonic phase, $\omega_k^2 = k^2 + \tilde{\omega}_0^2 > 0$.

Numerical results for \tilde{m}^2 and its representation in the two models are shown in fig. 5 for two values of ϕ_0 . We see that for $\phi_0 = 0.001 m_{\text{Pl}}$ the positive peaks are much narrower than for $\phi_0 = 0.1 m_{\text{Pl}}$; this agree with fig. 1, where the inflaton field spent much more time in the tachyonic region for smaller ϕ_0 . This leads us to expect that the delta fit should work better for $\phi_0 = 0.001 m_{\text{Pl}}$ than for $\phi_0 = 0.1 m_{\text{Pl}}$. In turn, the box fit might work better for $\phi_0/m_{\text{Pl}} = 0.1$.

The Floquet exponent of the delta model is given by

$$\mu_k = \frac{1}{T} \Re \operatorname{arcosh} \left[\cosh(\Gamma_k T) - \frac{\Lambda}{2\Gamma_k} \sinh(\Gamma_k T) \right], \quad \Lambda = 2\Gamma_0 \coth\left(\frac{\Gamma_0 T}{2}\right); \quad (3.9)$$

for the box model we find

$$\begin{aligned} \mu_k = \frac{1}{T} \Re \operatorname{arcosh} \left\{ [\cos(T_1 \tilde{\omega}_k) + \frac{\tilde{\Lambda}}{\tilde{\omega}_k} \sin(T_1 \tilde{\omega}_k)] \cosh(\Gamma_k T_2) \right. \\ \left. + \left[\frac{\Gamma_k^2 - \tilde{\omega}_0^2 + \tilde{\Lambda}^2}{2\Gamma_k \tilde{\omega}_k} \sin(T_1 \tilde{\omega}_k) + \frac{\tilde{\Lambda}}{\Gamma_k} \cos(T_1 \tilde{\omega}_k) \right] \sinh(\Gamma_k T_2) \right\}, \end{aligned} \quad (3.10a)$$

$$\tilde{\Lambda} = \tilde{\omega}_0 \tan\left(\frac{T_1 \tilde{\omega}_0}{2}\right) - \Gamma_0 \coth\left(\frac{T_2 \Gamma_0}{2}\right), \quad (3.10b)$$

with $T_2 = T - T_1$.

³Since a perfect step function has infinite derivative, many curve fitting routines will have difficulties. To circumvent this, we use the sigmoid function to mimic the logistic function with steepness parameter $\kappa = 500$.

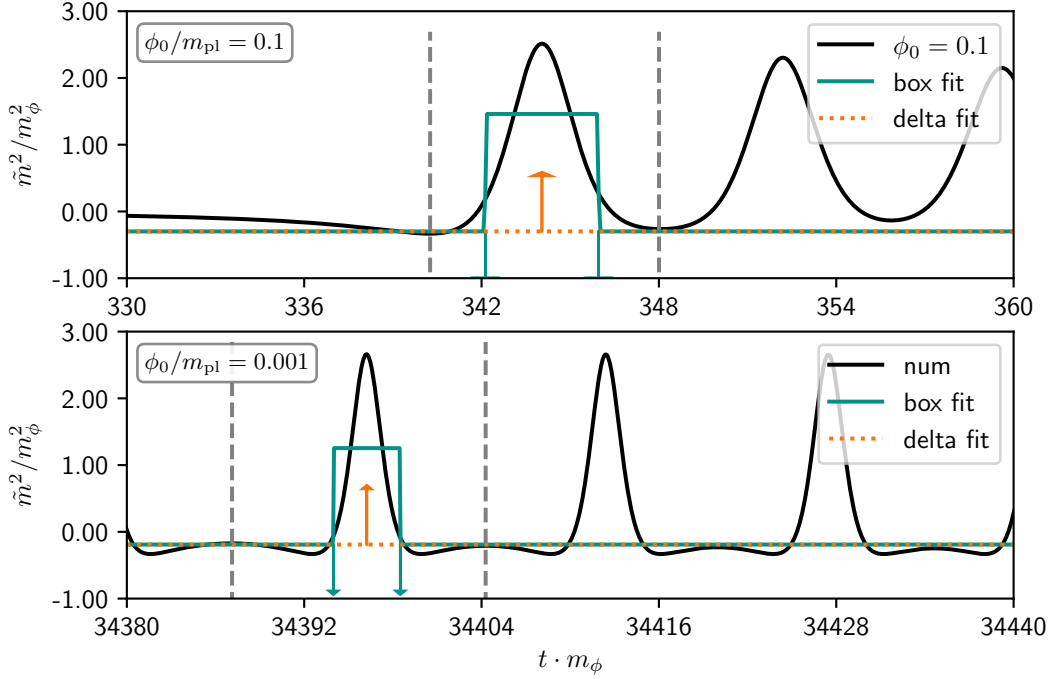


Figure 5: The smooth black lines show the effective squared inflaton mass $\tilde{m}^2(t)$ with $\phi_0 = 0.1 m_{\text{Pl}}$ (top) and $\phi_0 = 0.001 m_{\text{Pl}}$ (bottom), computed from solutions of the ordinary differential equation (2.10) with $H = 0$. In the delta model this is represented by the sum of a negative constant plus a delta-function at the location of the maximum of the effective mass (orange arrows). In the box model (blue) the fit jumps from a finite negative to a finite positive value, and subtracts delta-functions at the transition points in order to reproduce the dips beside the central peak (blue arrows). The fits are performed in the region enclosed by the gray dashed lines.

Examples of these analytical results are compared in fig. 6. to numerical results. For $\phi_0 = 0.1 m_{\text{Pl}}$ (top frame) both analytical approaches overestimate $\Re(\mu_k)$, but the delta model gets the location of the maximum k_{max} roughly right. The bad performance of the box model in this case might be due to the fact that the exact \tilde{m}^2 actually does not show pronounced dips close to the central peak in this case. On the other hand, both models describe the main instability band fairly well for $\phi_0 = 0.001 m_{\text{Pl}}$. The delta model does a little better here, but the box model also reproduces the second instability band quite accurately; this has also been observed in [37]. Both models reproduce the trend seen in fig. 4 that reducing ϕ_0 reduces k_{max} and increases the number of instability bands.

4 Lattice simulation

In order to accurately describe the non-linear dynamics we utilize lattice simulations. In the following subsection we describe the setup of our simulation. Focusing on $\phi_0 = 0.01 m_{\text{Pl}}$, in subsequent subsections we analyze the behavior of average field quantities, the Hartree approximation for the average field, the spectrum of fluctuations, and oscillons. In the final subsection we discuss the dependence on ϕ_0 .

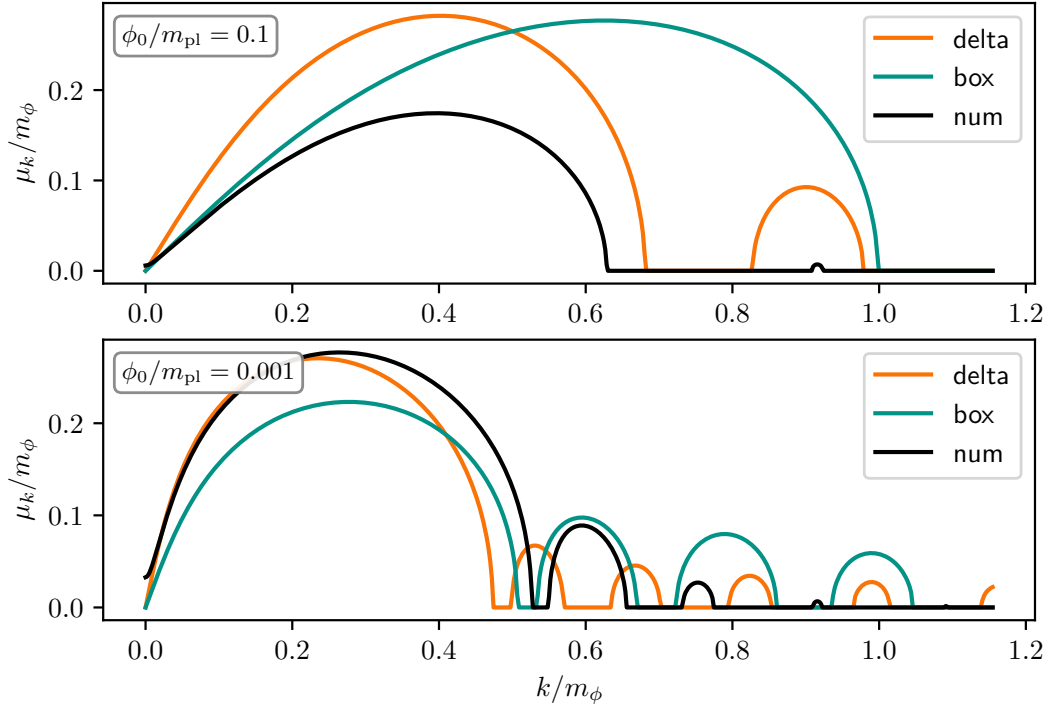


Figure 6: Floquet exponents as a function of k for $\phi_0 = 0.1 m_{\text{Pl}}$ (top) and $\phi_0 = 0.001 m_{\text{Pl}}$ (bottom). The black curves show numerical results, basically slices through the left frame of fig. 4. The orange and blue curves show analytical results based on the delta model, eq.(3.9), and the box model, eq.(3.10), respectively.

4.1 Simulation setup

We mainly use the program `CosmoLattice` [26] to simulate the dynamical evolution of the classical inflaton field. Some modifications to the program were made, but the core of the program stays intact. The program employs the following dimensionless variables:

$$\tilde{\phi} := \frac{\phi}{f_*}, \quad d\tilde{\eta} := a^{-\alpha}(\tilde{\eta})\omega_* dt, \quad d\tilde{x}^i := \omega_* dx^i. \quad (4.1)$$

Here t is the cosmic time and the x^i are comoving coordinates. In general the values of f_* , ω_* and α affect the numerical stability. We set f_* to ϕ_0 , which sets the order of magnitude of the oscillating background field at the beginning of the simulation. ω_* , which sets the unit of time and spatial distance and thus momentum, is chosen so that the oscillation period of inflaton is roughly of order of unity. The dynamics of inflation is often analyzed using conformal time, which corresponds to $\alpha = 1$. However, we are interested in the post-inflationary epoch. A simple oscillating field can easily be analyzed using the usual cosmic time, $\alpha = 0$. In the interesting field range all three terms in the inflaton potential contribute about equally, i.e. the oscillation is highly anharmonic, as we saw in fig. 1. Nevertheless we find that setting $\alpha = 0$ does not lead to any numerical late-time instability. Hence, we set

$$f_* = \phi_0, \quad \omega_* = \frac{\sqrt{d}}{3}\phi_0, \quad \alpha = 0. \quad (4.2)$$

We checked that setting $\alpha = 1$ leads to identical result. Our choice of f_* and ω_* implies that the dimensionless potential energy

$$\tilde{V} = \frac{V(\phi)}{f_*^2 \omega_*^2} \quad (4.3)$$

is basically independent of ϕ_0 . In order to avoid confusion, we will stick with $m_\phi = 6\omega_*$ as unit for length, time, and momentum when presenting results of the lattice simulation, just as we did in the previous chapters.

As discussed in Sec. 3.3, the initial fluctuations in momentum space are set according to the usual Bunch–Davis vacuum. Since we are working on a lattice with finite distance δx between neighboring grid points we must set a UV cutoff (**kCutoff**) for the initial fluctuations, beyond which they are set to zero. This “external” cutoff should be smaller than the implicit lattice cutoff $2\pi/\delta x$. Another important parameter is the overall size of the lattice, or the number of grid points (in one direction) N . For convenience, we set the infrared cutoff **kIR** instead of δx in the program input; they are related by

$$\delta x = \frac{2\pi}{N \text{ kIR}}. \quad (4.4)$$

The UV side of power spectra must always be checked at the end of the simulation. If **kCutoff** is too large, due to the discrete nature of lattice and thus periodicity in the reciprocal lattice, any dynamically generated super–UV modes get “reflected” to the infrared; this can cause a spurious enhancement at large wavelengths (small k).

We always use the velocity verlet method of order 4 (VV4) implemented in [26] to solve the differential equations. The accuracy of the simulation is quantified, as implemented in [26], by the relative difference of both sides of the second Friedmann equation, derived from the first Friedmann equation

$$H^2 = \frac{\rho_K + \rho_G + \rho_V}{3m_{\text{Pl}}^2}, \quad (4.5)$$

and from the ij -component of the Einstein equations:

$$\frac{a''}{a} = \frac{a^{2\alpha}}{3} \left(\frac{f_*}{m_{\text{Pl}}} \right)^2 [(\alpha - 2) \langle \tilde{\rho}_K \rangle + \alpha \langle \tilde{\rho}_G \rangle + (\alpha + 1) \langle \tilde{\rho}_V \rangle]. \quad (4.6)$$

ρ_K and ρ_V in eq.(4.5) have already been defined in eq.(2.12), and $\rho_G = (\nabla\phi)^2/(2a^2)$. In eq.(4.6), $\langle \dots \rangle$ denotes a volume averaged quantity, a prime denotes a derivative w.r.t. $\tilde{\eta}$, and the $\tilde{\rho}_i$ are the dimensionless energy densities defined via the rescaled variables of eq.(4.2):

$$\tilde{\rho}_K = \frac{1}{2} \left(\tilde{\phi}' \right)^2, \quad \tilde{\rho}_G = \frac{1}{2} \left(\tilde{\nabla} \tilde{\phi} \right)^2, \quad \tilde{\rho}_V = \tilde{V}. \quad (4.7)$$

For most of this chapter we will set

$$\phi_0 = 0.01 \, m_{\text{Pl}}; \quad (4.8)$$

the preceding discussion shows that this is one of the largest values of ϕ_0 where we can expect full–fledged nonlinear dynamics. We first tried starting our simulation at the (canonical) end of slow–roll inflation, where the second slow–roll parameter $|\eta_V| = 1$. The initial time derivative of the background field, $\dot{\phi}$, is computed from its equation of motion (2.10). However, we noticed that $\epsilon_V \ll 1$ for several more e–folds, which means that the fluctuations still play no role and just redshift away. We therefore switched to starting our lattice simulation at the time when $\ddot{a} = 0$,

computed from the numerical solution of the equation of motion (2.10). By the second Friedmann equation (4.6), this is equivalent to $(\dot{\phi})^2 = V(\phi)$; this happens slightly before the background field first crosses zero. Our final choices of the lattice parameters for different values of ϕ_0 can be found in appendix B.

Using eq.(4.6) as described above, we checked that the numerical error is kept within 10^{-8} throughout the simulation. However, since the expansion of the universe reduces the implicit UV cutoff on physical momenta we cannot completely avoid the problem of “reflecting” modes with large k into the IR region. Moreover, `CosmoLattice` does not include the backreaction of field inhomogeneities onto the metric, which is assumed to be given by the Friedman–Robertson–Walker form throughout. This means that the growth of overdensities due to gravitational attraction is not included. Due to these issues, the simulation eventually becomes physically unreliable, even if numerical errors remain small. We will come back to this later.

Note that we do not include the decay of the inflaton to other particles in our simulation. This is well justified if the inflaton couplings to other particles are small enough that they do not distort the inflaton potential through radiative corrections. As shown in [8] this implies $\Gamma_\phi < 10^{-14}m_\phi$ for $\phi_0 = 0.01 m_{\text{Pl}}$, where Γ_ϕ is the total (perturbative) decay width of the inflaton; for smaller ϕ_0 the upper bound on Γ_ϕ/m_ϕ is even smaller. Hence inflaton decay is certainly negligible during our simulation, which covers $t \lesssim 10^3/m_\phi$.

We are now ready to present some numerical results. We begin with a discussion of volume-averaged quantities.

4.2 Average quantities

We begin with fig. 7, which shows the volume-average of the inflaton field as a function of time (black) and additionally averaged over a couple of oscillations (blue). We see that at first the field oscillates as predicted by the solution of the equation of motion (2.10). During this epoch the amplitude of the oscillation, and the time-averaged field, decrease roughly as a negative power of time. This epoch lasts until $t \simeq 150m_\phi^{-1}$, which roughly matches the expectation of sec. 3.3. Then the mean field collapses, i.e. the oscillation amplitude decreases very quickly. Immediately after this collapse the volume-averaged field behaves more chaotically at short times scales, but its time-average continues to decline smoothly.

In order to gain insight into the collapse, we show the time evolution of the variance and skewness of the inflaton field in fig. 8. The variance, defined as

$$\langle \delta\phi^2 \rangle = \langle \phi^2 \rangle - \langle \phi \rangle^2, \quad (4.9)$$

describes the overall magnitude of the spatial variation of ϕ . The left frame of fig. 8, which uses a logarithmic y -axis, shows that it is initially very small, although growing roughly exponentially as expected from our Floquet analysis. For $50 \leq t \cdot m_\phi \leq 120$ the exponent is about $0.31/m_\phi$, which is less than twice the maximal Floquet coefficient shown in fig. 4; the factor of two arises since the variance is quadratic in the perturbation $\delta\phi$. We note that the variance oscillate along with the exponential growth. It is surprising, since the initial fluctuations are randomly seeded [26]. The same oscillation has been observed in [38, 39] as well. At $t \sim 150m_\phi^{-1}$, it reaches a maximum at $\sqrt{\langle \delta\phi^2 \rangle}/\phi_0 \sim 0.4$; we saw in fig. 7 that just before this time the amplitude of the oscillating $\langle \phi \rangle$ was only slightly above, and the time-averaged field somewhat below, this value. This means that in some regions of the lattice field fluctuations exceed the background field. Clearly the fluctuations can no longer be ignored at, and after, this time.

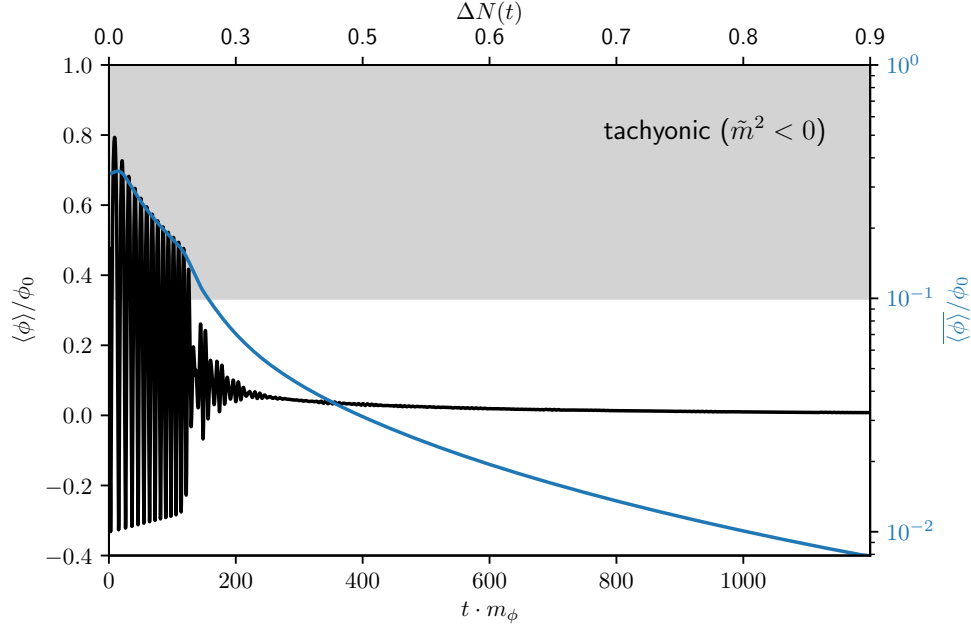


Figure 7: The black curve shows the evolution of the volume-averaged value of the inflaton field and refers to the linear left y -axis. The blue curve refers to the logarithmic right y -axis and gives the volume-averaged field value averaged over roughly two periods using a Gaussian filter. Two horizontal axes are given: one is the usual cosmic time t and the other is the number of e-folds after slow-roll inflation, i.e. it shows the evolution of the scale factor a . The tachyonic region, where the effective mass squared is negative, is shaded grey.

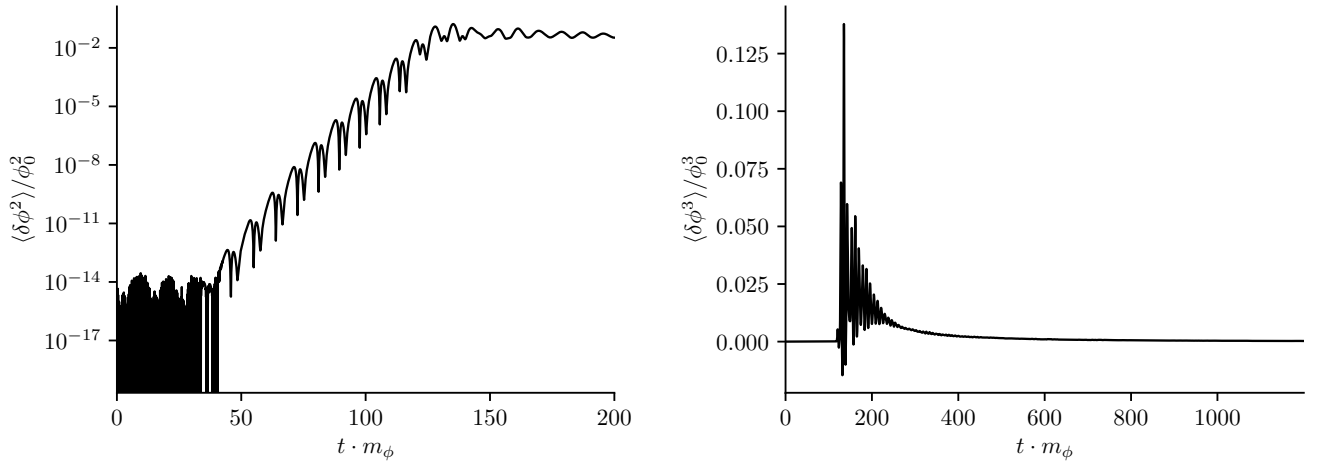


Figure 8: Variance and skewness of the inflaton field ϕ as function of cosmic time.

The skewness $\langle \delta\phi^3 \rangle$ is defined as

$$\langle \delta\phi^3 \rangle = \langle (\phi - \langle \phi \rangle)^3 \rangle = \langle \phi^3 \rangle - 3 \langle \phi \rangle (\langle \phi^2 \rangle - \langle \phi \rangle^2) - \langle \phi \rangle^3. \quad (4.10)$$

The right frame of fig. 8 shows that the skewness is positive most of the time, i.e. the spatial distribution of the field is skewed towards positive field values. This is expected, since the choice of a negative cubic coefficient in the inflaton potential (2.1) implies $V(|\phi|) < V(-|\phi|)$. Note also

that if the field fluctuation was purely Gaussian, any odd moment of the field, and hence also the skewness, would vanish. The non-zero three-point correlation here originates from the non-linear interaction.⁴ By using a linear y -axis in this figure, we demonstrate just how rapid the onset of the non-linear regime is.

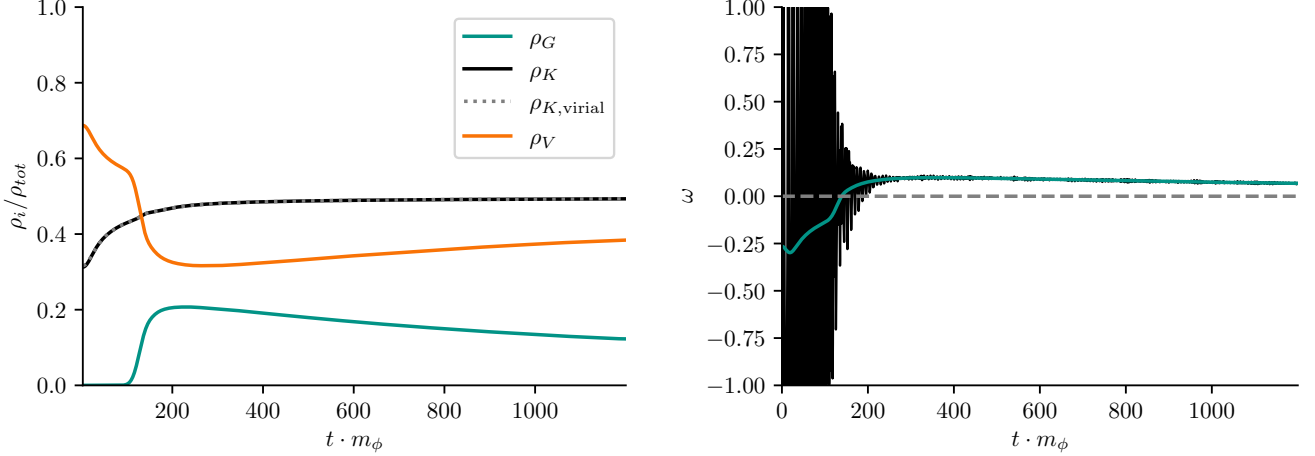


Figure 9: The left frame shows the potential energy ρ_V (red), kinetic energy ρ_K (black) and gradient energy ρ_G (blue) in units of the total energy, smoothed over roughly two periods of oscillations of the background field; the dotted gray curve (almost coinciding with the black curve) shows the virial prediction for the kinetic energy, eq.(4.11). The right frame shows the equation of state parameter ω (black) and its value smoothed over two periods (blue).

This can also be seen from the left frame of fig. 9, which shows the three contributions of eq.(4.5) to the total energy density, averaged over a couple of oscillations of the background field. We see that the gradient term remains negligible until just before the instance of collapse, but then very quickly becomes sizable. Initially, while the field inhomogeneities are small, the kinetic and potential energies oscillate out of phase with each other. In the linear approximation, i.e. for harmonic oscillations, their average values should be the same. Instead we see that initially the potential energy is about 50% larger, while after the collapse of the background field the kinetic energy gives the biggest contribution.

The gray dotted line in this figure is the prediction of the Virial theorem for the time averaged kinetic energy fraction:

$$\rho_{K,\text{virial}} = \langle \rho_G \rangle + d \left(2\phi_0^2 \langle \phi^2 \rangle - 4\phi_0 \langle \phi^3 \rangle + 2 \langle \phi^4 \rangle \right). \quad (4.11)$$

A heuristic derivation can be found in appendix C. During slow-roll inflation, $\rho_G = 0$ and $\phi \simeq \phi_0$. The virial theorem then predicts a very small ρ_K , which is indeed the case. In fact, the actual ρ_K closely tracks the prediction of the virial theorem during the entire simulation, including the time when the classical field collapses. We will come back to the issue of virialization in sec. 4.5.

The right frame of fig. 9 shows the equation of state parameter ω , computed from

$$\omega = \frac{p}{\rho} = \frac{\langle \rho_K \rangle - \langle \rho_G \rangle / 3 - \langle \rho_V \rangle}{\langle \rho_K \rangle + \langle \rho_G \rangle + \langle \rho_V \rangle}. \quad (4.12)$$

⁴Non-Gaussianity can also be tested by the kurtosis $\langle \phi^4 \rangle / \langle \phi^2 \rangle^2$. For purely Gaussian fluctuations this always equals 1 [40].

Of course, $\omega \simeq -1$ during inflation. We see that its time average remains negative as long as the backreaction is small, although $\omega > -1/3$ implies that the expansion of the universe is slowing down while the background field oscillates coherently. When the background field collapses, ω becomes positive but quite small, $\omega \lesssim 0.1$; it very slowly decreases later on. Hence the assumption $\omega = 0$ frequently made in analyses of reheating if the inflaton potential is quadratic near the origin is not a bad approximation, but might not be good enough when trying to precisely relate the reheat temperature and the number of e-folds of inflation after CMB scales left the horizon, usually called N_{CMB} .

4.3 Hartree approximation

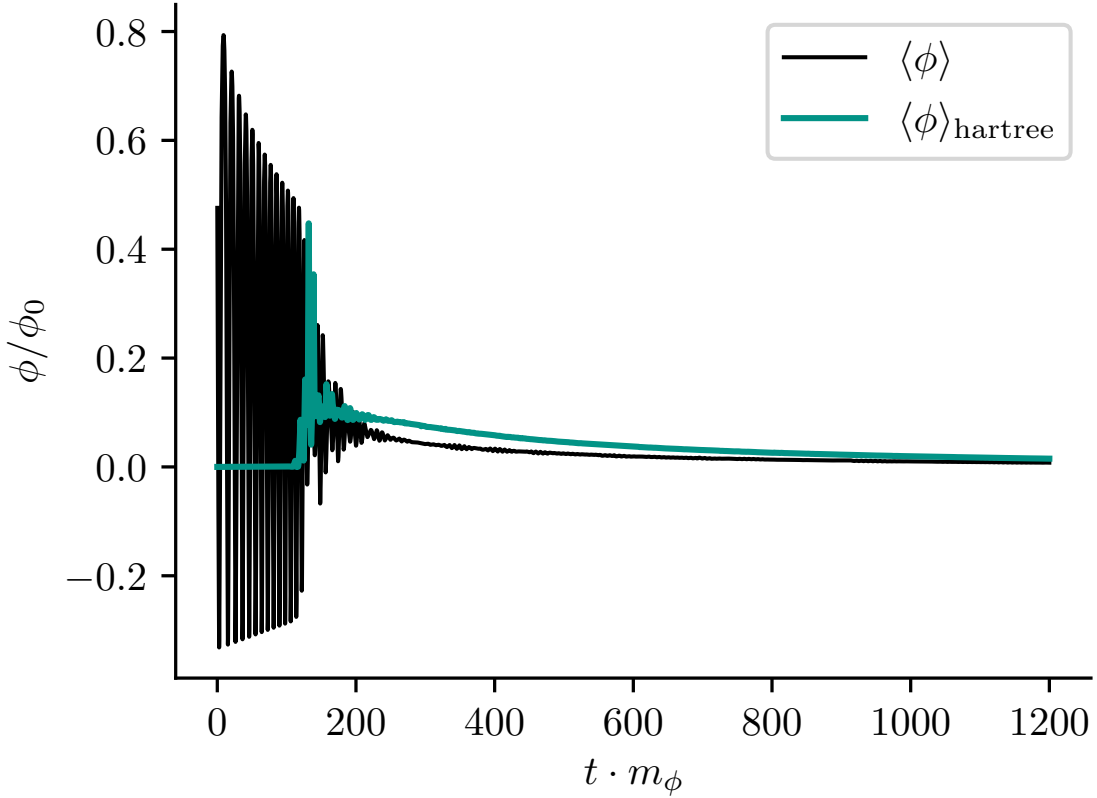


Figure 10: The black curve again shows the evolution of the background field as computed from our lattice simulation, as in fig. 7. The blue curve shows the value of the background field $\langle\phi\rangle$ that minimizes the Hartree potential (4.14).

In this subsection we describe a first attempt to analyze the backreaction of the fluctuations onto the mean field $\langle\phi\rangle$. To that end we decompose the scalar field into the homogeneous part and the perturbations:

$$\phi(x, t) = \langle\phi\rangle(t) + \delta\phi(x, t), \quad (4.13)$$

where $\langle\delta\phi\rangle = 0$ by definition. We insert this ansatz into the inflaton potential (2.1), and keep terms that are at least linear in $\langle\phi\rangle$ (the constant term doesn't influence the evolution of the background field). Finally, we employ the Hartree approximation, i.e. we average over the volume, which

removes terms linear in $\delta\phi$. This yields:⁵

$$V_{\text{Hartree}} = d \left[\langle\phi\rangle^4 - \frac{8}{3}\phi_0 \langle\phi\rangle^3 + \langle\phi\rangle^2 (2\phi_0^2 + 6 \langle\delta\phi^2\rangle) + \langle\phi\rangle (4 \langle\delta\phi^3\rangle - 8\phi_0 \langle\delta\phi^2\rangle) \right]. \quad (4.14)$$

The result depends on the variance $\langle\delta\phi^2\rangle$ and skewness $\langle\delta\phi^3\rangle$ that we had shown in fig. 8. There is a positive contribution to the coefficient of $\langle\phi\rangle^2$ which will increase the mass of the background field; however, the left frame of fig. 8 shows that this effect is significant only for $150 \lesssim t \cdot m_\phi \lesssim 200$. In contrast, the term linear in $\langle\phi\rangle$ is new. Fig. 8 shows that the second, negative, contribution usually dominates. It moves the minimum of the potential away from zero, to a field value $\langle\phi\rangle_{\text{Hartree}} \lesssim 2 \langle\delta\phi^2\rangle / \phi_0$.

The result is shown in fig. 10. Of course, $\langle\phi\rangle_{\text{Hartree}}$ does not oscillate. However, it allows to understand why $\langle\phi\rangle$ increases again slightly just after its initial collapse, and describes its long-term behavior semi-quantitatively. Since we had to take $\langle\delta\phi^2\rangle$ and $\langle\delta\phi^3\rangle$ from our simulation in order to compute $\langle\phi\rangle_{\text{Hartree}}$, this does not allow ab initio understanding of the behavior of $\langle\phi\rangle(t)$ during and after the collapse. However, it is a useful consistency check on our simulation.

4.4 Field fluctuation spectrum

Next we consider the Fourier modes of the field and density perturbations. Although the power spectrum cannot capture all the properties of the lattice results (e.g. there is definitely non-Gaussianity present), it is still worth investigating. In the following, the power spectrum is defined via the two-point correlation function in Fourier space [26]:

$$\langle f(\vec{k}) f(\vec{k}') \rangle = (2\pi)^3 \frac{2\pi^2}{k^3} \mathcal{P}_f(k) \delta^{(3)}(\vec{k} - \vec{k}'). \quad (4.15)$$

Here f can be any scalar quantity, e.g. the field ϕ itself or an energy density, defined in Fourier space. Note that rotational symmetry has been assumed, hence the power only depends on the absolute value $k = |\vec{k}|$. The power can be used to directly compute the second moment of f in coordinate space:

$$\langle f^2 \rangle = \int d \log k \mathcal{P}_f(k). \quad (4.16)$$

The power spectrum of inflaton field fluctuations is shown in the left frame of fig. 11. We see that only modes with $k \lesssim m_\phi$ show rapid (exponential) growth at the beginning of the simulation (red curves); this agrees with our previous linear analysis in sec. 3. As expected, modes with $k \sim 0.3m_\phi$ grow fastest, see fig. 4b. In between the first two curves, i.e. in the first $t = 30 m_\phi^{-1}$ of the simulation, this mode grows by roughly 5 orders of magnitude. On the other hand, the Floquet analysis (see e.g. fig. 4) predicts

$$\mathcal{P}_\phi(k) \propto \exp(2\Re\mu_k \Delta t), \quad (4.17)$$

with $\Re\mu_k \simeq 0.26m_\phi$ for $k = 0.3m_\phi$, or a growth factor of $4 \cdot 10^6$ in this case. It is not surprising that the Floquet analysis over-estimates the growth somewhat, since the full lattice simulation takes into account the energy loss of the background field due to Hubble friction as well as the redshift effect; both effects tend to reduce the amount of amplification.⁶

⁵We neglect terms $\propto \beta$, which are only important if $\langle\phi\rangle$ is very close to ϕ_0 .

⁶In addition, there is a subtlety in the Floquet analysis, related to the periodic functions $A(t)$ and $B(t)$ in eq.(3.1). If one measures the growth rate in a time period which is not an integer multiple of the period, then the time dependence of these periodic functions influence the result.

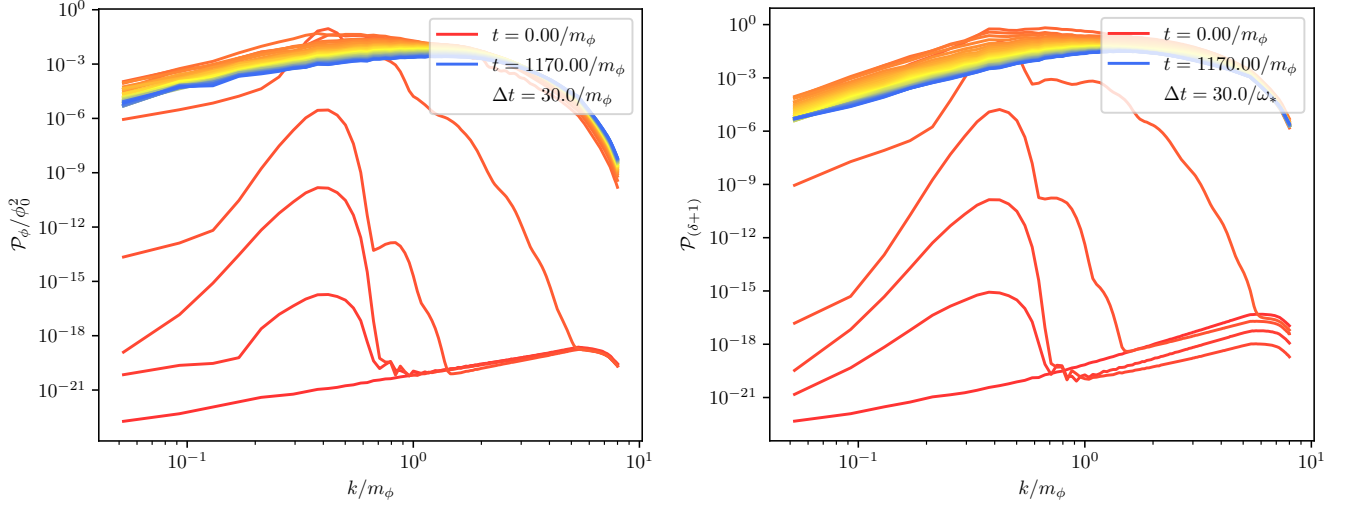


Figure 11: The power spectrum of the inflaton field (left) and of the relative energy density $\rho(x)/\langle\rho\rangle = \delta(x) + 1$ (right) as function of the comoving momentum on a log–log scale. The color of the curve indicates when the spectrum is taken; from early to late time: red, yellow and blue.

At later times modes with larger k also begin to grow rapidly, as can be seen from the fourth and fifth red curves in fig. 11. Recall that the condition for tachyonic instability is $\omega_k^2 = k^2/a^2 + \tilde{m}^2 < 0$, so the excitation of modes with higher comoving momentum is partly due to the redshift.

At $t \approx 120 m_\phi^{-1}$, the spectrum reaches a peak value $\lesssim 10^{-1}/\phi_0^2$, which is comparable to the square of the background field value shown in fig. 7. The brief time window afterwards when the excited modes get more evenly distributed across all (available) momenta can be understood as re-scattering [7]. Then the spectrum slowly moves to the UV. Recall, however, that we plot the spectrum vs. the co-moving momentum k , the physical momentum q being smaller by a factor $a(t)$; recall that we set $a = 1$ at the beginning of our simulation. Physical momenta redshift by a factor ~ 2.5 in the course of our simulation. The peak of the power spectrum at $k \sim 2m_\phi$ at the end of our simulation (blue curve in fig. 11) therefore corresponds to $q \sim 0.8m_\phi$. Nevertheless this can be regarded as first indication that quite small structures appear; we will see shortly that this is indeed the case.

The right frame of fig. 11 shows the relative energy density power spectrum. It is again calculated from eq.(4.15), with f now being the density contrast

$$\delta(x) = \frac{\rho(x) - \langle\rho\rangle}{\langle\rho\rangle} = \frac{\rho(x)}{\langle\rho\rangle} - 1. \quad (4.18)$$

Qualitatively the curves are similar to those in the left frame. Quantitatively the modes with $k \gtrsim m_\phi$ grow a little faster. The energy density gets a contribution from the kinetic energy, which is naturally associated with somewhat larger values of k .

4.5 Oscillons

Clearly our system shows quite non-trivial dynamics, due to the inflaton self interactions. We therefore expect distributions to be quite non-Gaussian. Moreover, we saw at the end of the previous subsection an indication for the formation of relatively small structures. The latter can be investigated most directly by looking at the lattice itself. To that end, we take “snapshots” of the

distribution of the (total) energy density across the lattice. From it, other quantities, for example probability distribution functions, can be extracted.

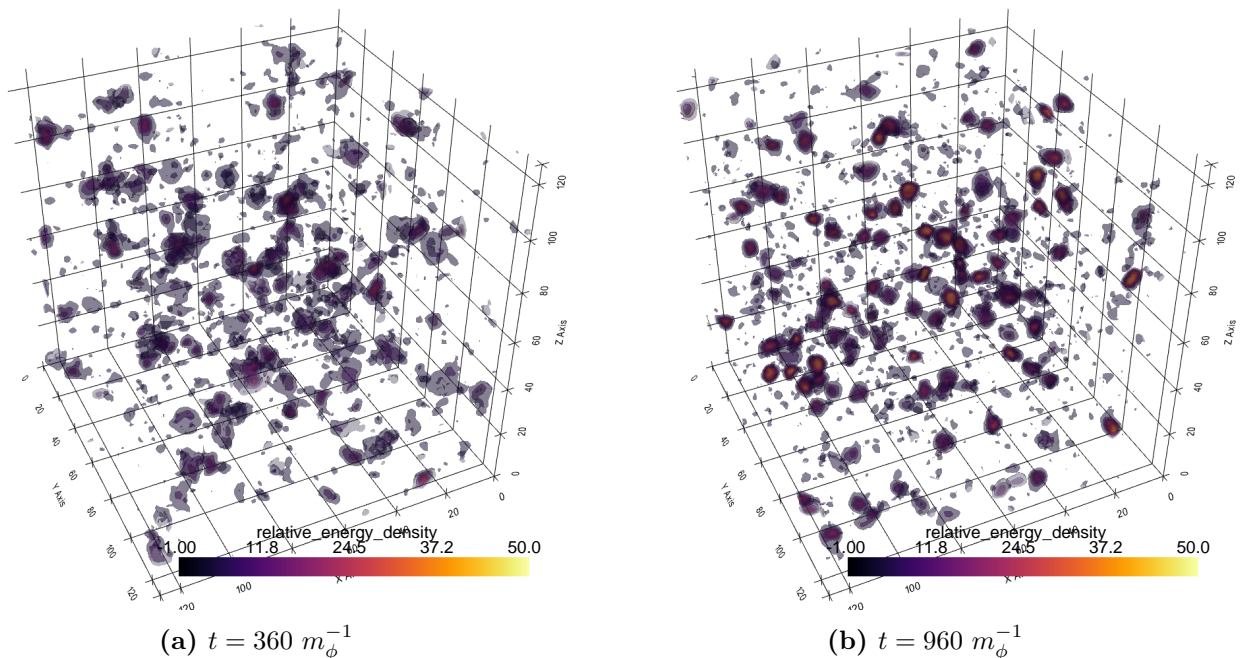


Figure 12: Isosurfaces of relative energy densities $\rho(x)/\langle\rho\rangle$ predicted by the lattice simulation at two different times. The axes denote comoving spatial coordinates in terms of the lattice spacing δx ; in physical units, $\delta x \simeq 0.6/m_\phi$. For better visualization, only 1/8th of the volume of the whole lattice is shown here.

Figure 12 shows two such snapshots, taken after the collapse of the initial, homogeneous field but before the fragmentation process completely settled down. Already in the left frame, taken at $t = 360/m_\phi$, small quasi spherical lumps are formed; some of them have central relative energy density $\rho(x)/\langle\rho\rangle \gtrsim 20$. Note that although these objects are highly localized, they are not stationary; some tend to move around. Indeed, there is nothing to forbid them from having a velocity.

By $t = 960/m_\phi$ (right frame) these lumps have shrunk further; in some cases the central overdensity now exceeds 30. At this later time the typical size of these lumps is about 5 lattice units; from eqs.(4.2) and (4.4), and the values given in table 2 in Appendix B, we see that $\delta x \simeq 0.6/m_\phi$ in physical (albeit comoving) units. A size of $3/m_\phi$ corresponds to $k \simeq 2\pi \cdot (m_\phi/3) \simeq 2m_\phi$. We saw in fig. 11 that the late time density contrast power spectrum indeed peaks at about this value of k . This is just a qualitative consistency check; we will analyze the size distribution of these overdense regions more quantitatively towards the end of this subsection.

These objects can be identified as oscillons, which are non-topological solitons with rapidly oscillating core [41–43]. Unlike its close relative, the Q -ball of complex scalar field, an oscillon is not associated with an exactly conserved charge and thus not infinitely stable (by Derrick’s theorem [44]).

Nevertheless, under certain conditions, it has been known for some time that a scalar field can fragment into such quasi-stable configuration [43]. Of course, this requires nontrivial self-interactions of this field; in particular, the potential needs to be shallower than quadratic over an

extended range of field values [9].⁷ Our potential, given in eq.(2.1), clearly satisfies this condition for $\phi > 0$, where the cubic term is negative; indeed, as we emphasized in sec. 2, the potential has negative curvature for $1/3 < \phi/\phi_0 < 1$, see eq.(2.7). Note, however, that our potential is *steeper* than quadratic for $\phi < 0$. This is not the first time that oscillons have been observed in a highly asymmetric potential, see [45].

Earlier studies using symmetric potentials found that oscillons can be surprisingly stable, with lifetime up to $10^8 m_\phi^{-1}$. This is well beyond the end of our simulation. In fact, since oscillons have roughly constant physical size, our lattice becomes too coarse to simulate them at $t \gg 10^3/m_\phi$. However, we see no reason why our oscillons shouldn't decay eventually. In the known examples they eventually transition to outgoing waves [43, 46–48]. Recall from our discussion at the end of sec. 4.1 that in our model perturbative decay of the inflaton only happens at $t \geq 10^{14}/m_\phi$. It seems safe to assume that all oscillons will have disappeared well before that time.

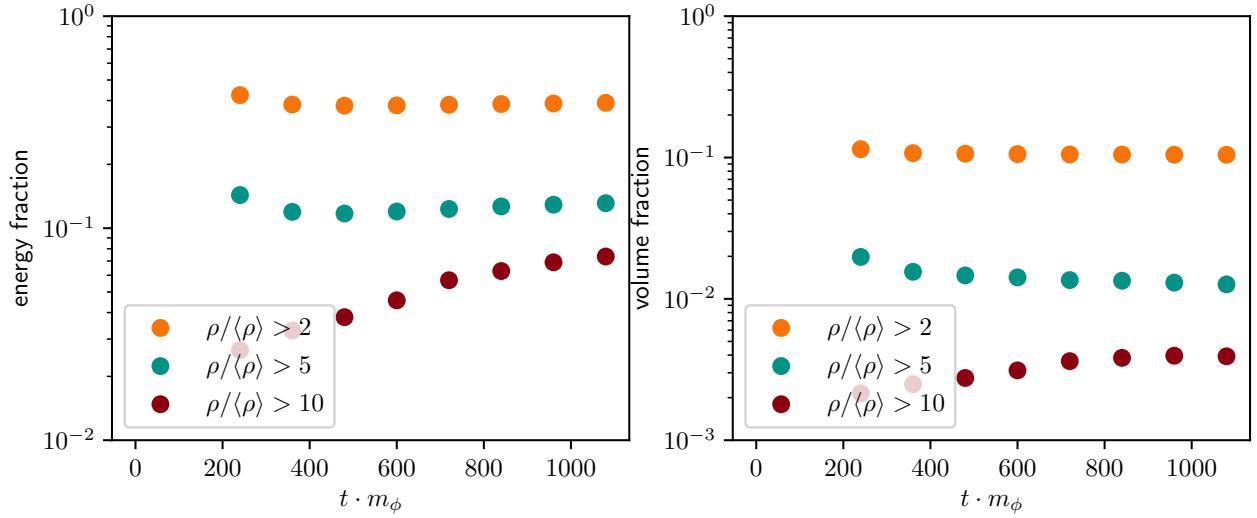


Figure 13: Fraction of energy (left) and volume (right) of regions where the energy density exceeds the overall average by at least a factor of 2 (orange), 5 (blue) and 10 (dark red).

In order to understand the impact of oscillon formation more quantitatively, we inspect which fraction of the energy these compact objects contribute, and how much space they occupy. Results for $t \geq 200 m_\phi^{-1}$ are shown in fig. 13. We produced these results by simply scanning over all the points in the lattice; a given point contributes (e.g.) to the orange curves if the local density is at least twice the global average. Prior to the collapse of the background field, the inhomogeneities (resulting from quantum fluctuations) are very small. Regions with overdensity of more than 100% (orange) first appear at $t \simeq 20 m_\phi^{-1}$, but fill only $\sim 3 \cdot 10^{-6}$ of the total volume. At $t = 40 m_\phi^{-1}$, still well before the times covered in fig. 13, nearly 5% of points have more than 100% overdensity, and about 0.1% of points have density more than 10 times the average value, shown in dark red in the figure. Much later, at $t \simeq 800 m_\phi^{-1}$, the system enters a quasi-stable configuration, where $\sim 30\%$ of the energy of the whole lattice is stored in localized regions with $\delta(x) = \rho/\langle\rho\rangle - 1 > 1$; these regions only occupy $\sim 10\%$ of the volume.

⁷To see this in a crude way, consider a localized field configuration in one dimension: $\phi(x, t) = \Phi(x) \cos(\omega t)$. The equation of motion implies $-\omega^2 \Phi - \partial_x^2 \Phi + V'(\Phi) = 0$. Away from the center of the configuration, one can take $V'(\Phi) \sim m^2 \Phi$, as the non-linearity should not be relevant. In order to have a localized configuration one needs to have positive curvature, $\partial_x^2 \Phi > 0$, near its boundary; this requires $\omega^2 < m^2$. In the center, however, we expect a maximum, i.e. $\partial_x^2 \Phi < 0$. In order to achieve this while $\omega^2 < m^2$, one must have $V'(\Phi) < m^2 \Phi$.

The results of fig. 13 only show the total contribution of all overdense regions. Ideally we would want to track individual oscillons. Unfortunately, this is not so easy, since they are quite small but move around fairly quickly. In order to at least partially tackle this problem, we employ Density-Based Spatial Clustering of Applications with Noise (DBSCAN) from `sklearn` [22]. We only consider oscillons that have $\rho/\langle\rho\rangle > 10$ somewhere in their volume. We then label all nearby points where $\rho/\langle\rho\rangle > 5$. DBSCAN is used to group these points into discrete clusters. This gives at least a rough idea of the energy contained in, and size of, individual oscillons. One advantage of DBSCAN is the ability to remove anomalies, so that some small non-oscillon fluctuations can be excluded. Of course, the criterion for such anomalies must be given by hand.

The energy and (comoving) radius of each oscillon are computed in the following way:

$$E = \sum_{\text{cluster}} (\delta x)^3 \rho, \quad (4.19a)$$

$$R_c = \left(\frac{3}{4\pi} \sum_{\text{cluster}} 1 \right)^{1/3} \delta x; \quad (4.19b)$$

in the second equation we have implicitly assumed that oscillons are spherically symmetric. In both equations the sum is taken over all the points in one cluster from DBSCAN. At any given time (with $t \geq 360 m_\phi^{-1}$) there will be many such clusters in our lattice. Their energies are plotted versus their radii in fig. 14.

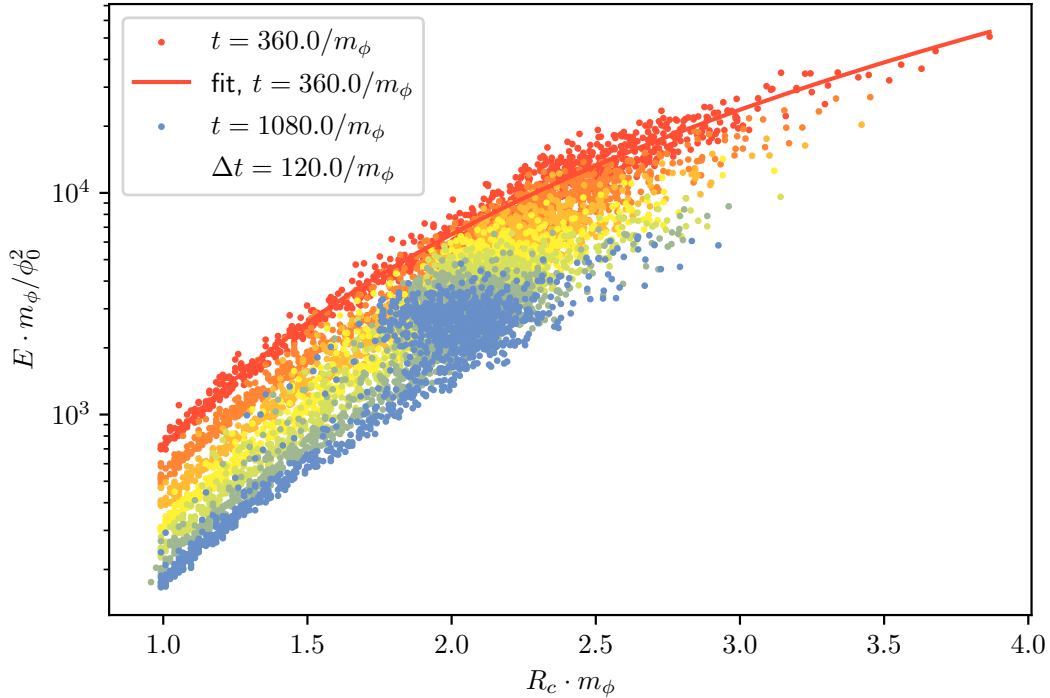


Figure 14: Energy and (comoving) radius R_c of oscillons taken at different times. Oscillons are identified and isolated using the DBSCAN algorithm. The criterion for oscillons used here is a high overdensity, $\rho/\langle\rho\rangle > 10$, and we consider nearby points with $\rho/\langle\rho\rangle > 5$ to belong to the same oscillon. The choice of other DBSCAN parameters doesn't affect the result much; here we choose $\text{eps} = 3$ and $\text{min-samples} = 20$.

We see that initially, i.e. at $t = 360 m_\phi^{-1}$, the algorithm finds quite a broad spectrum of cluster sizes and energies. These results can be described quite well by a power law, $E \propto R_c^{3.19}$. The

exponent only slightly deviates from 3, indicating that the configurations have nearly constant average energy density. Recall, however, that at this time the system hasn't settled into a near-equilibrium yet; among other things, we do not expect the lumps to be strictly spherically symmetric.

The conventional wisdom is that non-linear localized structures don't get much affected by the expansion of spacetime, similar to galaxies in the expanding Universe. Since we lack the ability to track each individual oscillon a definite statement cannot be made. However, fig. 14 clearly shows that the energy of most oscillons decreases quite significantly with time. This agrees with ref. [49], where a spherical lattice simulation is used to trace one single oscillon for a long time ($\mathcal{O}(10^5)$ oscillations), for a hilltop-shaped inflaton potential. In their simulation a given oscillon can lose almost half of its initial energy while the Universe expands by a factor of 5.

Another intriguing feature of fig. 14 is that gradually over-dense regions seem to move to $R_c \approx 2m_\phi^{-1}$ and $E \cdot m_\phi / \phi_0^2 \approx 2000$; see the blue dots. Evidently many over-dense lumps relax into this relatively stable configuration after fragmentation; some of the lumps with lower radius and energy might even be artifacts of the DBSCAN algorithm.

Ref. [43] found that the typical radius of an oscillon is $R_c \sim 3m_\phi^{-1}$. As noted above, in our case the lattice spacing can be related to the inflaton (rest) mass via equation (4.4). Here we find roughly similar typical size of lumps. Quantitatively our oscillons appear to be slightly larger, taking into account that the scale factor in the FRW metric increases by a factor ~ 2.5 in the course of our simulation. We note, however, that the oscillation frequency, measured in units of m_ϕ , also appears to be slightly lower than in ref. [43], indicating that our effective mass (for the purposes of oscillon physics) is slightly smaller than that in the (quite different) potentials analyzed in this earlier reference.

We finally recall that our system remains virialized even while the background field collapses, as noted in section 4.2. This is consistent with the observation in ref. [43] that oscillons are virialized attractor field configurations.

4.6 Dependence on ϕ_0

It is time to check the effect of changing ϕ_0 , which is basically the only free parameter of our model, on the preheating and oscillon dynamics.

We first note that the system remains virialized at all times for all values of ϕ_0 we investigated, i.e. the kinetic energy averaged over a couple of oscillations agrees very well with the prediction of the virial theorem, as in fig. 9.

As expected from results in section 3, for large ϕ_0 the perturbations do not grow long enough to significantly alter the background evolution. For example, we saw in fig. 1 that for $\phi_0 = 0.1 m_{\text{Pl}}$ the Hubble friction is so large that the background field only enters the tachyonic region a few times. Hence the exponential growth of the field fluctuation, whose spectrum initially again peaks around $k = m_\phi / \sqrt{3}$, already ends at $t \simeq 30 m_\phi^{-1}$. This is confirmed by fig. 15. Here we also see that at later times the power in perturbations decreases again, due to the continuing expansion of the universe.

The collapse of the background field occurs only for $\phi_0 \lesssim 0.02 m_{\text{Pl}}$. The dynamics here is already similar to that of our benchmark point $\phi_0 = 0.01 m_{\text{Pl}}$. For even lower values of ϕ_0 the dynamics remains qualitatively the same, although some quantitative differences do occur. In the following we show some results for $\phi_0 = 10^{-4} m_{\text{Pl}}$.

The left frame of fig. 16 shows the evolution of the background field; it should be compared with fig. 7. The collapse of the background field again happens at $t \simeq 100 m_\phi^{-1}$, since the increase of the term $\propto \ln(m_{\text{Pl}}/\phi_0)$ in eq.(3.4) is compensated by the slight increase in $\Re(\mu_k)$, see fig. 4b. However, recall from the discussion of eq.(2.12) that $H/m_\phi \propto \phi_0$. Hence the expansion of the universe during

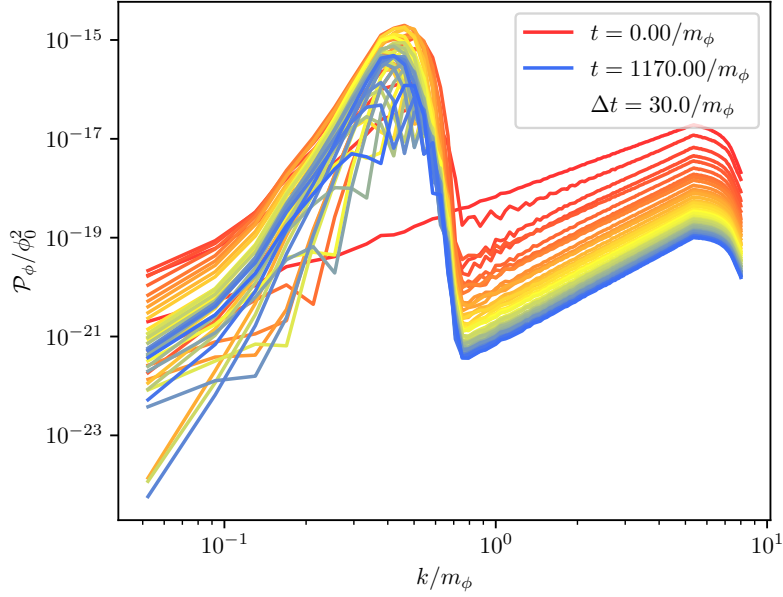


Figure 15: Field fluctuation power spectrum for $\phi_0 = 0.1 m_{\text{Pl}}$.

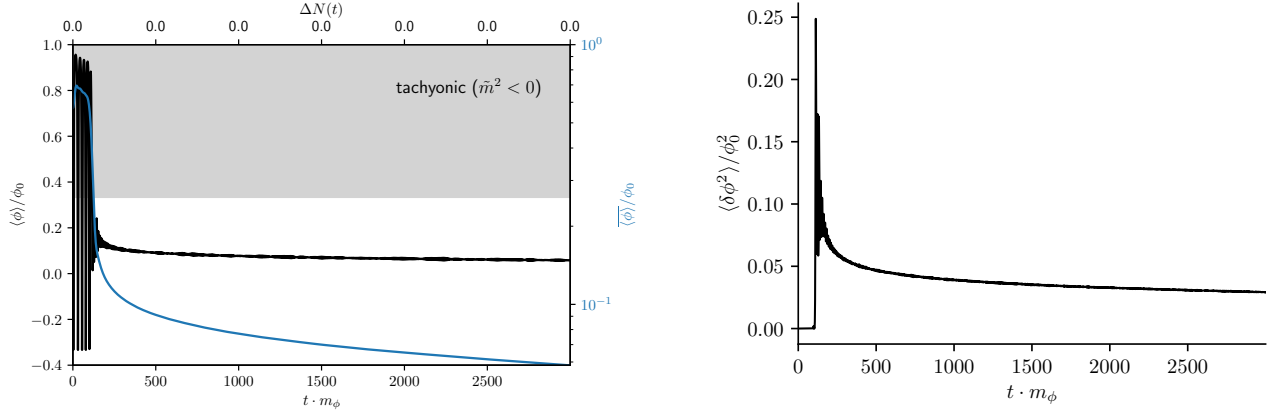


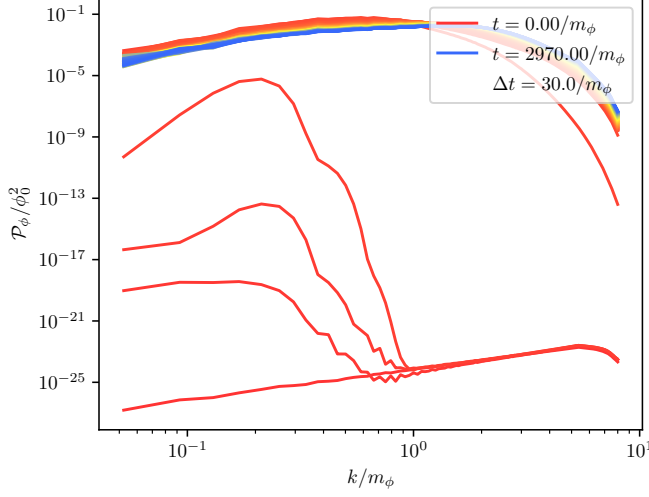
Figure 16: The spatial average of the inflaton field (left) and of its variance (right), for $\phi_0 = 10^{-4} m_{\text{Pl}}$.

the simulation, shown by the upper horizontal axis in the left frame of fig. 16 in terms of e -folds, is negligible in this case, compared to an expansion by a factor of 2.5 for $\phi_0 = 0.01 m_{\text{Pl}}$.

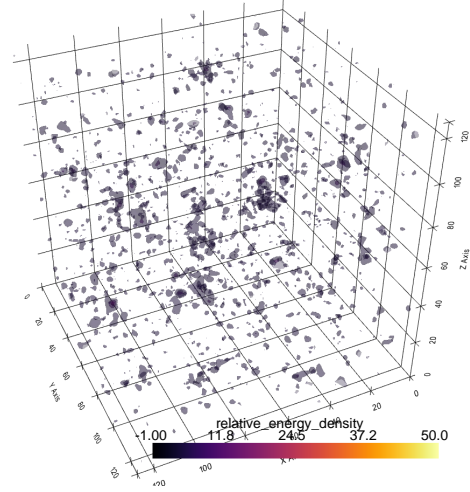
The right frame of fig. 16 shows the variance of the inflaton field ϕ , c.f. the left frame of fig. 8 which however uses a logarithmic y -axis. The peak of the variance in units of ϕ_0^2 is somewhat higher for $\phi_0 = 10^{-4} m_{\text{Pl}}$ (0.25 vs. 0.175); more importantly, in these units the variance stays near 0.05 throughout the simulation, whereas it quickly drops to about 0.02 for $\phi_0 = 10^{-2} m_{\text{Pl}}$.

The evolution of the power spectrum is depicted in fig. 17a. We see that initially the amplified modes always have comoving $k \lesssim m_\phi / \sqrt{3}$; due to the lack of expansion the comoving k remains very close to the physical one in this case. The fastest growth occurs for $k \simeq 0.2 m_\phi$, in agreement with the results of our Floquet analysis shown in fig. 4. Modes with $k > m_\phi$ get excited only in the nonlinear regime, once $\delta \phi_k \sim \langle \phi \rangle$. At late times the peak value of $\mathcal{P}_\phi / \phi_0^2$ is slightly higher than for $\phi_0 = 10^{-2} m_{\text{Pl}}$.

The right frame of fig. 17 shows a snapshot of the total energy density at $t = 1200 m_\phi^{-1}$. Comparing with fig. 12 we see a lower typically density contrast of $\lesssim 10$. The overdense regions



(a) Power spectrum of fluctuations.



(b) Snapshot of the energy density contrast in 1/8th of the lattice at $t = 1200 m_\phi^{-1}$.

Figure 17: Power spectrum and snapshots for $\phi_0 = 10^{-4} m_{\text{Pl}}$.

(oscillons) here are typically also smaller when measured in units of m_ϕ^{-1} . Earlier numerical studies of oscillons have found that their size and lifetime can depend very sensitively on their initial core density [9, 43]. However, these simulations typically start from a single oscillon with high initial density, and are thus not directly comparable to our simulation where the initial condition is very smooth.

5 Observational consequences

Our results so far show that for $\phi_0 \lesssim 0.02 m_{\text{Pl}}$ the inflaton field becomes very inhomogeneous and fragments into oscillons. This happens at a time scale of $\sim 100 m_\phi^{-1}$, well before the perturbative decay of the inflatons that reheats the universe. It is important to ask whether this rather violent early dynamics can have observable consequences.

We already saw in fig. 9 that the fragmented system has slightly positive equation of state parameter ω , while $\omega = 0$ for an inflaton field oscillating coherently around a quadratic minimum. As a result, the Universe expands slightly more slowly; recall that the scale factor $a \propto t^{2/(3+3w)}$. This affects the number of e-folds before the end of inflation when a given perturbation first exited the horizon. However, this also depends strongly on the reheat temperature, which can vary over a considerable range in this model [8].

Recall also that earlier numerical studies found that oscillons live for at most $\sim 10^8 m_\phi^{-1}$ before they decay by emitting inflaton particles [43, 46, 50]. If this result carries over to our model, oscillons decay well before (free) inflatons do. This indicates that the self resonance and oscillons have negligible effects [43] on the reheating dynamics. In the end, reheating will complete as usual, via perturbative channel(s).

Nevertheless there are two possible messengers from the very early universe, primordial black holes and gravitational waves. We will discuss them in the subsequent subsections.

5.1 Primordial black holes

We saw in the previous section that large density contrasts can be generated after the fragmentation. Here we analyze whether they could seed black hole formation. If small black holes are produced, their evaporation can impact reheating, and could even be its main mechanism. At the same time, light black holes can also be a source of relics, e.g. dark matter particles.

We begin our argument by showing that the timescale for gravitational collapse cannot be shorter than that for the fragmentation of the inflaton field. For a static Universe, overdensities grow exponentially by gravitational attraction, with typical timescale (Jeans instability) [51]

$$t_J = \frac{1}{\sqrt{4\pi G\rho}} = \frac{\sqrt{2}m_{\text{Pl}}}{\sqrt{\rho}} \frac{1}{\sqrt{\delta+1}} = \frac{1}{H} \frac{\sqrt{2}}{\sqrt{3(\delta+1)}}. \quad (5.1)$$

Here ρ denotes the average energy density of a small (over-dense) patch of the Universe and $\langle\rho\rangle$ is the average energy density inside a Hubble horizon.⁸ Therefore, if we assume that the density contrast cannot exceed unity by more than a factor of 30 or so, we have

$$t_J \gtrsim \frac{\sqrt{2}}{10H} > \frac{\sqrt{2}}{10H_I} \simeq \frac{m_{\text{Pl}}}{m_\phi\phi_0}. \quad (5.2)$$

Since nonlinear effects appear in the inflaton dynamics only if $\phi_0 \lesssim 0.01 m_{\text{Pl}}$, the inequality (5.2) implies $t_J \gtrsim 100 m_\phi^{-1}$ for parameters that lead to the fragmentation of the inflaton field. Hence gravitational collapse cannot be faster than the collapse of the inflaton condensate into a highly inhomogeneous configuration.

If PBHs are ever produced, then their masses will be

$$M_{\text{BH}} = \frac{4\pi}{3} R^3 \rho_{\text{local}}, \quad (5.3)$$

where R is the typical extension of over-dense regions and ρ_{local} their energy density. From our lattice simulation,

$$R_o \simeq 2m_\phi^{-1}. \quad (5.4)$$

Moreover, neglecting the expansion of space,

$$\rho_{\text{local}} \sim 10 \langle\rho\rangle = 30m_{\text{Pl}}^2 H_I^2. \quad (5.5)$$

Inserting eqs.(5.4) and (5.5) into eq.(5.3) yields a mass of a single oscillon that is independent of ϕ_0 :

$$M_o \simeq 320\pi \frac{m_{\text{Pl}}^2 H_I^2}{m_\phi^3} \sim 2 \cdot 10^3 \text{ g}. \quad (5.6)$$

No gravitational collapse would be needed if a single oscillon already contained sufficient mass inside its radius to form a black hole. The Schwarzschild radius of a (non-rotating) black hole is given by [52]

$$r_S = \frac{2}{8\pi} \frac{M}{m_{\text{Pl}}^2}. \quad (5.7)$$

⁸There should be an additional term containing the sound speed in the denominator. However, it increases the time scale of the gravitational instability.

Estimating the oscillon mass from eq.(5.6), the oscillon radius of eq.(5.4) is smaller than the Schwarzschild radius of eq.(5.7) if

$$\phi_0/m_{\text{Pl}} \gtrsim 1. \quad (5.8)$$

Recall that oscillons only form if $\phi_0 \lesssim 0.01 m_{\text{Pl}}$, in which case the oscillon radius is at least two orders of magnitude larger than the Schwarzschild radius.

Hence PBH formation would require the merger of many oscillons through gravitational dynamics. This would have to occur while oscillons still exist, i.e. at $t \lesssim 10^8 m_\phi^{-1}$. The maximal mass of a black hole formed at time t is given by the energy within one Hubble radius, $1/H(t) = 3t/2$ deep in a matter-dominated epoch ($w = 0$).⁹ At such late time the dilution of the energy density $\propto a^{-3}$ has to be taken into account. Recalling our convention $a(t_0) = 1$ we have

$$a(t) = \left[\frac{3}{2} H(t_0)(t - t_0) + 1 \right]^{\frac{2}{3(1+w)}}. \quad (5.9)$$

For example, for $t - t_0 = 10^8 m_\phi^{-1}$ and taking $H(t_0) = H_I$, we have

$$a(t = 10^8/m_\phi)^3 \simeq 10^{16} \left(\frac{\phi_0}{4m_{\text{Pl}}} \right)^2. \quad (5.10)$$

The mass inside a Hubble radius, $M_H(t) \simeq H(t)^{-3} \rho_I a(t)^{-3}$, could then be estimated as

$$M_H(t = 10^8/m_\phi) \sim 10^8 M_o \left(\frac{m_{\text{Pl}}}{\phi_0} \right)^2. \quad (5.11)$$

A primordial black hole would have to have a mass of a few times 10^{15} g at least in order to not decay by Hawking radiation before the present time [53]. Eqs.(5.11) and (5.6) show that this might conceivably happen for all $\phi_0 \lesssim 0.01 m_{\text{Pl}}$ where oscillons form. In contrast, since the lifetime of a black hole scales with the third power of its mass, a single oscillon somehow collapsing into a black hole would evaporate after $\sim 10^{-19}$ seconds.

Of course, eq.(5.11) only gives a crude upper bound on the mass of any PBH that might conceivably form out of merging oscillons. The mass inside a Hubble horizon (at appropriately chosen time) is also used in the Press–Schechter formalism, which automatically includes the gravitational collapse of over-dense regions at later times. However, usually it is applied to *superhorizon*, *Gaussian* curvature perturbations; neither of these two requirements is met here. There are some arguments that the PS formalism might still apply in more general situations [54–56], which however do not include oscillons. It seems to us that the formation rate of PBHs in our scenario can be estimated reliably only using methods of full numerical relativity [11, 12]. Some attempts have been made in [10, 57–59]. Recently, a full-fledged numerical relativity simulation of oscillons has been done; it seems unlikely for black hole to form in such scenarios [60].

5.2 Gravitational waves

The formation of black holes is an intrinsically non-perturbative process. Unfortunately we lack the computational resources to derive quantitative results beyond the simple estimates presented in the previous subsection. In contrast, the production of gravitational waves can be treated perturbatively in many cases. Moreover, they do not decay, nor are they diluted or otherwise significantly modified

⁹In this simple estimate we ignore the deviation of w from zero.

by the later evolution of the universe, apart from the kinematic redshifting due to the Hubble expansion.

In this subsection we first briefly review the theory of gravitational wave production from a scalar field in the (very) early universe. We then compute the peak frequency of, and the energy density carried by, primordial gravitational waves in our model.

5.2.1 Theory

This section reviews the basics of gravitational waves (at first order), mostly based on [61]. Consider the metric composed of the FRW background and a small perturbation in the comoving frame:

$$g_{\mu\nu} = a^2(\eta)(\eta_{\mu\nu} + h_{\mu\nu}). \quad (5.12)$$

We use the gauge freedom to set the temporal components as well as the trace and “divergence” of h to zero:

$$h_{\mu 0} = 0, \quad h_i^i = 0, \quad \partial_i h_{ij} = 0. \quad (5.13)$$

This is known as the transverse–traceless (TT) gauge. With this gauge choice, we go from ten degrees of freedom to only two. The physical results discussed below are gauge-independent to the order considered [61].

One can decompose the metric perturbation into irreducible representations of $\text{SO}(2)$. The symmetric transverse traceless part h_{ij} has helicity -2 and should be interpreted as gravitational waves [51]. The energy–momentum tensor can also be decomposed into helicity sectors; the helicity -2 part is $T_{ij}, i \neq j$. For an ideal fluid the off-diagonal entries of T_{ij} vanish, so that h_{ij} is decoupled from the energy–momentum tensor. But if one relaxes this condition, one obtains [61]

$$\ddot{h}_{ij} + 3H\dot{h}_{ij} - \frac{\nabla^2}{a^2}h_{ij} = \frac{2}{m_{\text{Pl}}^2}\Pi_{ij}^{TT}; \quad (5.14)$$

Π_{ij}^{TT} is the transverse-traceless part of the anisotropic tensor Π_{ij} , defined via

$$a^2\Pi_{ij} = T_{ij} - pg_{ij}. \quad (5.15)$$

For a single real scalar field ϕ one has [61, 62]

$$\Pi_{ij}^{TT} = (\partial_i\phi\partial_j\phi)^{TT}. \quad (5.16)$$

Note that this term vanishes in a perfectly spherically symmetric system, in accordance with Birkhoff’s theorem [63]. The over-dense regions created in the fragmentation of the inflaton background field break this symmetry; in fact, as shown in the previous sections, even a single such region is usually not perfectly spherically symmetric, especially at early times. We therefore expect GWs to be produced when the inflaton field fragments into oscillons. They will give rise to a background of stochastic gravitational waves.

In order to quantify the magnitude of this contribution, one needs to go the second order in metric perturbation. The effective energy–momentum tensor of GWs is obtained by averaging the second order Ricci tensor. Its 00 component is

$$\rho_{\text{gw}} = T_{\text{gw}}^{00} = \frac{m_{\text{Pl}}^2}{4} \langle \dot{h}_{ij}\dot{h}^{ij} \rangle, \quad (5.17)$$

where the average is taken over length scales. In order to decide whether this can be detected, one should consider the spectrum of GWs rather than the integrated energy density:

$$\Omega_{\text{gw}}(t) = \int \frac{1}{\rho_c(t)} \frac{d\rho_{\text{gw}}(k, t)}{d \log k} d \log k := \int \Omega_{\text{gw}}(k, t) d \log k . \quad (5.18)$$

Here $\rho_c(t) = 3m_{\text{Pl}}^2 H^2(t)$ is the (time dependent) critical energy density.

ρ_{gw} redshifts like radiation. As shown in appendix D, a gravitational wave produced with comoving wave vector k_{gw} now has frequency [10]

$$f_0 = \frac{1}{2\pi} \frac{k_{\text{gw}}}{a_p} \frac{a_p}{a_0} \simeq \frac{k_{\text{gw}}}{a_p} \frac{1}{\rho_p^{1/4}} \cdot 4.00 \times 10^{10} \text{Hz} , \quad (5.19)$$

where the subscript p denotes the time when gravitational waves were produced whereas the subscript 0 refers to the present time. The scaled energy density Ω_{gw} is constant during the radiation dominated epoch, but becomes smaller in the matter and dark energy dominated epochs, so that today,

$$\Omega_{\text{gw},0} \simeq 8.00 \times 10^{-6} \cdot \Omega_{\text{gw},p} . \quad (5.20)$$

It should be noted that the approximation used in appendix D assumes a very short reheating period; the results then don't depend on the reheating temperature. As shown in appendix E this is not a bad approximation for high reheat temperature T_R ; however, for lower T_R the frequency and scaled energy density of primordial GWs might be further reduced by a couple of orders of magnitude.

5.2.2 Analytical Estimates

Our model has basically only a single free parameter, ϕ_0 . It determines the mass of the inflaton, which in turn sets the scale for the size of the overdense regions, as we saw above. We therefore write $k_{\text{gw}} = \tilde{k}_{\text{gw}} m_\phi$, where the dimensionless quantity \tilde{k}_{gw} should be of order unity if the typical wavelength of GWs at production is comparable to the size of an oscillon. Since during the fragmentation of the inflaton field the universe expands by less than one e-fold, we take $\rho_p \simeq \rho(\phi = \phi_0) \simeq V(\phi_0)$. Then we obtain from eq.(5.19), setting $a_p = 1$:¹⁰

$$f_0 \simeq \tilde{k}_{\text{gw}} \sqrt{\frac{\phi_0}{m_{\text{Pl}}}} \cdot 1.60 \times 10^7 \text{Hz} . \quad (5.21)$$

Hence, smaller ϕ_0 leads to lower frequency GW signals, potentially in the sub MHz range.

It is conjectured that at production the relative energy density of GWs can be written as [40, 64]

$$\frac{\rho_{\text{gw,tot}}}{\rho_{\text{tot}}} = \alpha \left(\frac{H}{k} \right)^2 , \quad (5.22)$$

where the ‘‘fudge factor’’ α should be order of unity for a sufficiently inhomogeneous medium emitting GWs. The current scaled GW energy density can then be estimated as

$$\Omega_{\text{gw},0} h^2 \simeq 1.00 \times 10^{-7} \left(\frac{\phi_0}{m_{\text{Pl}}} \right)^2 \frac{\alpha}{\tilde{k}_{\text{gw}}^2} . \quad (5.23)$$

¹⁰Recall that we set the scale factor $a = 1$ at the start of our simulation.

5.2.3 Numerical Results

The evolution of the metric perturbation h_{ij} is computed numerically by discretizing eq.(5.14); the GW energy density can then be obtained from eq.(5.17). Finally, today's GW frequency and energy density can be computed from eqs.(5.19) and (5.20), respectively [65, 66].

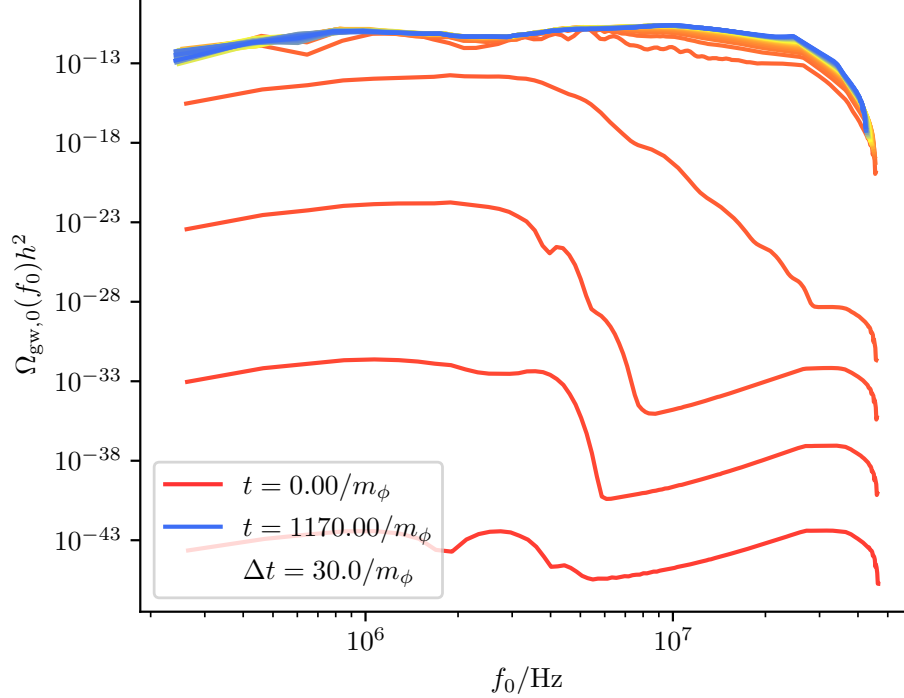


Figure 18: Today's GW energy density per logarithmic frequency interval in terms of today's frequency for $\phi_0 = 0.01 m_{\text{Pl}}$. Today's reduced Hubble constant is taken to be $h = 0.674$ [3]. Each curve shows the contribution of GWs produced up to the time shown.

Results for $\phi_0 = 0.01 m_{\text{Pl}}$ are shown in fig. 18. We saw in fig. 11 that initially field fluctuations with $k \lesssim m_\phi/2$ grow exponentially due to the tachyonic instability. This gives rise to gravitational waves with (today's) frequency $\lesssim 5$ MHz. The broader, but less pronounced peak in the GW spectrum at frequencies of tens of MHz is sourced later, during the epoch of linear growth of fluctuations and their back-reaction on the inflaton condensate [14, 16]. Once oscillons are fully formed, they become quite spherical; as argued above, a single oscillon will then not produce significant amounts of GW any more, explaining the saturation of the curves at later times [7, 10].¹¹

In fig. 19 we show the (final) GW energy density for three values of ϕ_0 , along side with sensitivity curves of some future experiments; the latter are taken from ref.[67]. As indicated in eq.(5.21), the peak of the GW spectrum decreases with decreasing ϕ_0 . Numerically the scaling is slower than $f_{\text{peak}} \propto \sqrt{\phi_0}$. Moreover, as predicted by eq.(5.23) Ω_{gw} quickly decreases with decreasing ϕ_0 . Unfortunately the GWs have peak frequency of several MHz, out of reach for currently planned next-generation GW detectors; some ideas for detecting such high frequency GWs are discussed in [68]. Note also that the irreducible gravitational wave background from perturbations of the

¹¹The motion of the various oscillons relative to each other does not end once oscillons are fully formed. However, the typical time scale for that is much longer than that for the very rapid field oscillations inside the oscillons – hence their name, after all. Therefore the GWs produced in the encounters of separate oscillons have much lower energy density, and remains essentially invisible on the logarithmic scale of fig. 18.

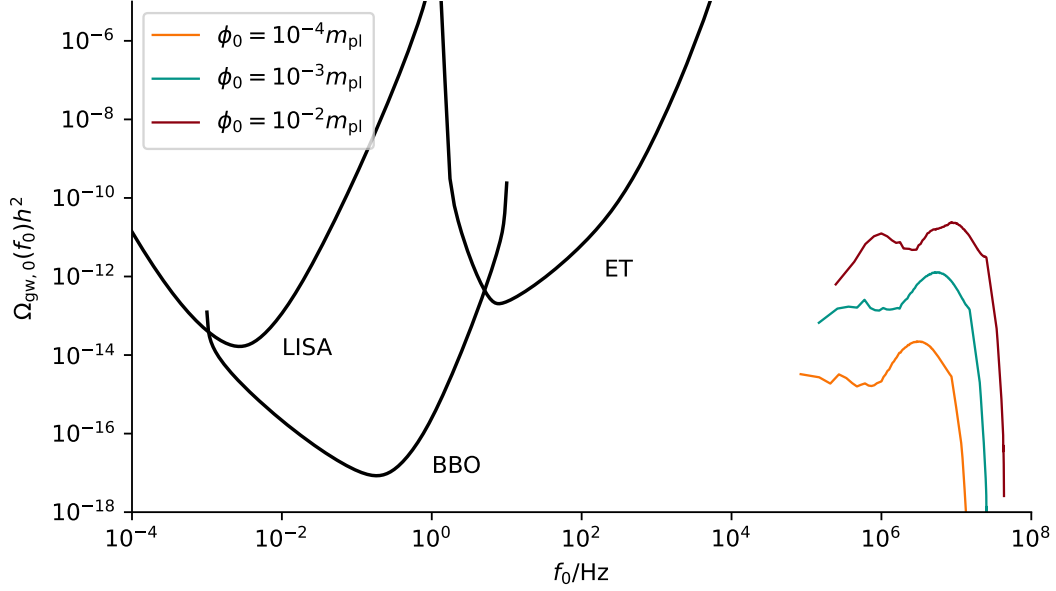


Figure 19: The colorful curves show GW signals for three values of ϕ_0 ; these correspond to the topmost curve shown in fig. 18, i.e. they show the total of all GWs emitted during our simulation. For comparison, sensitivity curves for future experiments [67] are shown in black.

metric during inflation, customarily parameterized by r , is constrained by CMB experiments in the $10^{-19} - 10^{-17}\text{Hz}$ range [61]. Thus, the high frequency gravitational waves could provide us the complementary evidence of the dynamics of the inflaton field on the opposite side of the spectrum.

Depending on the equation of state of the system between fragmentation and the end of thermalization, the curves shown in fig. 19 can move around somewhat. In particular, slow thermalization, i.e. a low reheat temperature, implies extra expansion, in which case the gravitation waves would have smaller frequency (longer wavelength) and smaller energy density in today's Universe, see appendix E.

5.2.4 Gravitational waves contribution to dark radiation

Gravitational waves contribute to the radiation field as far as the expansion history of the universe is concerned. Any measurement of the background evolution can therefore in principle constrain the total energy density carried by gravitational waves. This is usually expressed by the effective number of neutrino generations N_{eff} (after e^+e^- annihilation).

Processes in the early universe freeze out at temperature T where $\Gamma(T) \simeq H(T)$. In particular, the weak interactions between neutron and proton freeze out at $T \sim 1$ MeV, the exact temperature being sensitive to the expansion rate at that time. The freeze-out temperature determines the neutron to proton ratio which in turn determines the primordial ^4He abundance, since almost all neutrons end up in ^4He . Here we assume that the photon to baryon ratio, which also affects BBN dynamics, is determined from CMB data, which impose further constraints on N_{eff} . Altogether, $N_{\text{eff}} < 3.2$ at 95% confidence level [69] corresponding to $\Omega_{\text{gw},0}h^2 < 1.12 \times 10^{-6}$ [61].¹²

The spectra shown in fig. 19 can be integrated via eq.(5.18). The resulting total scaled energy

¹²There are two conditions for this constraint to apply. First, the GWs must be produced before BBN. Second, the GWs must be sub-horizon at the time of BBN. Since the GWs considered here are produced after inflation, they remain inside the horizon until the present time.

density in and today's peak frequency of the gravitational waves produced by the collapse of the homogeneous inflaton field are collected in table 1, for four different values of ϕ_0 .

ϕ_0/m_{Pl}	$f_{\text{max},0}/\text{Hz}$	$\Omega_{\text{gw},0}h^2$
1.00×10^{-2}	8.81×10^6	2.05×10^{-11}
5.00×10^{-3}	6.92×10^6	7.91×10^{-12}
1.00×10^{-3}	5.25×10^6	8.79×10^{-13}
1.00×10^{-4}	3.00×10^6	1.57×10^{-14}

Table 1: Today's peak frequency and integrated scaled energy density of GWs produced just after the end of inflation, for various values of ϕ_0 .

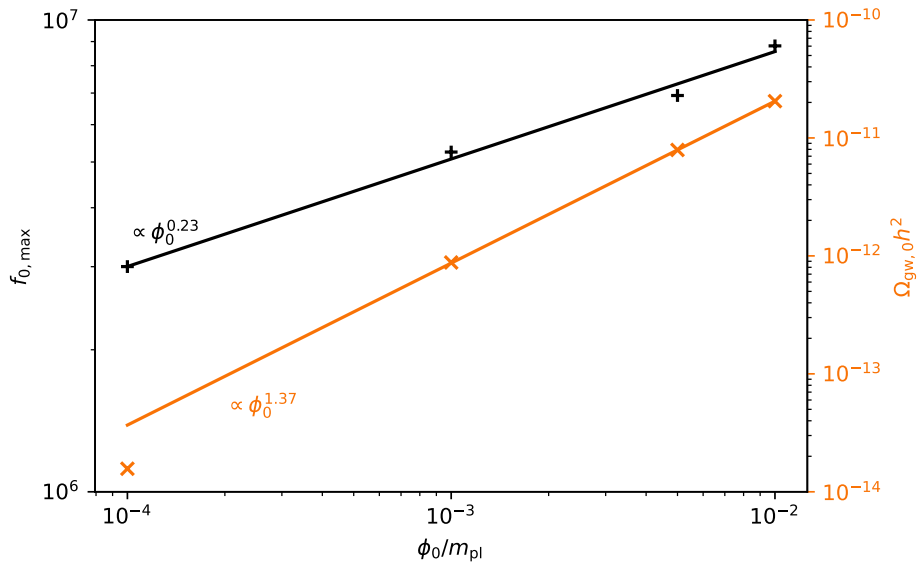


Figure 20: Power law fits of today's peak frequency and integrated energy density of GWs produced just after inflation.

The scaling of $f_{0,\text{max}}$ and $\Omega_{\text{gw},0}h^2$ with ϕ_0 are somewhat weaker than in the simple analytical estimates of eqs.(5.21) and (5.23). They do nevertheless exhibit power law behavior, as shown in fig. 20. There is additional ϕ_0 dependence “hidden” in \tilde{k}_{gw} and α which partly compensates the decline of $f_{\text{max},0}$ and Ω_{gw} with decreasing ϕ_0 . On the other hand, we saw in sec. 4.6 that for $\phi_0 \gtrsim 10^{-2} m_{\text{Pl}}$ the expansion of the universe during the epoch of GW production is not negligible, hence the assumption $\rho_p \simeq V(\phi_0)$ is not well warranted; this strengthens the dependence of $f_{\text{max},0}$ on ϕ_0 . In any case, fig. 20 shows that $\Omega_{\text{gw}}h^2$ is more than four orders of magnitude below the present bound; its impact on the overall evolution of the universe will therefore remain undetectable for the foreseeable future.

6 Conclusion

In this work we investigated the post-inflationary non-perturbative dynamics of the inflaton sector in a simple, renormalizable model with a polynomial potential featuring a near inflection point at field value $\phi = \phi_0$. As in (nearly) all successful models of small field inflation, the second

derivative of the inflaton potential is negative during inflation. In our model the inflaton field re-enters this tachyonic regime many times if the parameter $\phi_0 \lesssim 10^{-1} m_{\text{Pl}}$. As a result field fluctuations with comoving wave vector $k \lesssim m_\phi/2$ grow exponentially; here m_ϕ is the physical mass of inflaton particles. As long as the back-reaction of the perturbations on the inflaton background can be neglected the problem can be solved approximately using Floquet analysis. The numerical results, in terms of Floquet exponents, tell us how fast this growth is; see fig. 4. One can also estimate the time of back-reaction, see eq.(3.4); at this time the background field fragments, and the exponential growth of perturbations ends. Note that even before this time the Floquet calculation involves several approximations, hence the results cannot be fully trusted especially when ϕ_0/m_{Pl} is relatively large. Analytically, this is a hard problem, partly due to the nature of the potential since quadratic, cubic and quartic terms are of comparable importance in the tachyonic regime. An attempt has been made by fitting the effective mass as a function of time. The height and position of the dominant peak as well as the multiple bands in the Floquet map can be reproduced for small ϕ_0 with a simple box model, see fig. 6.

For large ϕ_0 the Hubble friction quickly dampens the oscillations of the background field, so that the exponential growth of fluctuations soon comes to an end. On the other hand, for $\phi_0 \lesssim 0.02 m_{\text{Pl}}$, the fluctuations become large enough to significantly alter the background field evolution, i.e. the back-reaction time is shorter than the time during which the (unperturbed) background field accesses the tachyonic regime. In this non-perturbative regime, lattice simulation is necessary and `CosmoLattice` [26] has been used. Once the field fluctuations start to dominate the background, the field fragments, see fig. 11, and non-linear soliton-like objects are formed, see fig. 12. They are often called oscillons and can be very long-lived, compared to the natural time scale of the dynamics which is set by $1/m_\phi$. For our benchmark point $\phi_0 = 0.01 m_{\text{Pl}}$ we computed the typical radius and energy density of these oscillons, see fig. 14; our results qualitatively agree with similar results in the literature for different potentials. It is worth noting that in contrast to a lot of previous studies, e.g. [14, 49, 70–72], our inflaton potential is very asymmetric around $\phi = 0$; in particular, its second derivative is negative only for positive $\phi \in]\phi_0/3, \phi_0[$.

We saw that after the background field fragments, large fractions of the total energy density are stored in the gradient and kinetic energies. Nevertheless the system remains virialized throughout. The equation of state parameter ω becomes slightly positive, see fig. 9. The background evolution after the collapse can be explained semi-quantitatively using the Hartree approximation, see fig. 10. These features remain qualitatively the same for yet smaller values of ϕ_0 , as shown in sec. 4.6. However, the oscillon size and energy seem to decrease somewhat with decreasing ϕ_0 , even when measured in units of the appropriate power of m_ϕ .

The inflaton fluctuations are highly non-Gaussian, see fig. 8. However, these perturbations are of sub-horizon size after the end of inflation; the relevant length scales are well below those probed by common cosmological observations like the CMB anisotropies or even the Lyman- α forest. Moreover, we expect that these inhomogeneities will be smoothed out once the inflatons decay, which in our model happens well after the oscillons decay by radiating inflaton particles.

Our lattice computation does not include gravitational effects. Conceivably the large density fluctuations created when the inflaton field fragments could seed primordial black hole formation. We showed that a single oscillon will not collapse into a black hole; however, this does not exclude the possibility that the gravitational attraction between oscillons, which was ignored in our simulation, could eventually trigger gravitational collapse. We also noted that black holes formed from a single, or a few, oscillons would decay well before BBN via Hawking radiation. However, if most of the energy density inside a Hubble radius at the end of the oscillon lifetime should end up in a single black hole, it would be sufficiently heavy to survive until today. While this scenario does not appear

very likely to us, non-perturbative computation including gravity are likely necessary in order to settle this question.

In the turbulent phase when the background field fragments, gravitational waves will be generated. They are (mostly) emitted during oscillon formation, and are thus of sub-horizon size. As a result, the predicted peak of the spectrum today lies in the MHz range, which is very difficult to probe. Moreover, the energy density of these gravitational has negligible impact on the expansion history of the universe, see figs. 19 and 20.

There are many avenues for possible future work. It might be possible to improve the analytical understanding of the epoch of exponential growth before back-reaction becomes important, via a more sophisticated Floquet analysis. As already emphasized, we could not make reliable prediction concerning the possible formation of primordial black holes. To that end, computations in numerical relativity will be required, see e.g. [11, 12]. Moreover, our numerical resources did not allow us to extend the simulation beyond $\mathcal{O}(10^3) m_\phi^{-1}$. We expect interactions between oscillons to continue at later times, possibly leading to clustering and merging of oscillons [72, 73]. In fact, we do not even know just how long our oscillons will survive even in the absence of gravity.

In summary, we have shown that even in a renormalizable, small-field model featuring a single real inflaton field the dynamics of the epoch immediately following inflation can be very complicated. If the model parameter $\phi_0 \lesssim 10^{-2} m_{\text{Pl}}$, the inflaton field quickly fragments into long-lived oscillons, leading to the production of primordial gravitational waves at MHz frequencies, and perhaps even to the formation of primordial black holes.

Acknowledgement

We would like to thank Yong Xu and Mustafa A. Amin for useful discussions. Our gratitude also goes to the CosmoLattice team. We appreciate that the physics department of University Bonn provides us the computing cluster for the lattice simulation.

A Details of the Floquet analysis

Here, we try to describe the detailed computation of Floquet exponents. This part is largely based on [32].

A.1 Finding the period

In principle, one can find the period by computing the integral

$$T = \sqrt{2} \int_{\phi_{\min}}^{\phi_{\max}} \frac{d\phi}{\sqrt{\rho_{\text{tot}} - V(\phi)}}. \quad (\text{A.1})$$

If we take $\rho_{\text{tot}} = V(\phi_0)$ and take $1 - \beta \approx 1$, we need to evaluate the integral

$$T = \sqrt{\frac{6}{d}} \frac{1}{\phi_0} \int_{x_{\min}}^{x_{\max}} \frac{dx}{\sqrt{1 - 3x^4 + 8x^3 - 6x^2}}, \quad (\text{A.2})$$

where the new dimensionless variable $x = \phi/\phi_0$ has been introduced. x_{\max} and x_{\min} are the maximal and minimal field value in one oscillation. This integral does converge as long as $x_{\max} < 1$. It is however, not so trivial to determine x_{\min} and x_{\max} analytically. For practical purposes, the period is determined by solving the homogeneous differential equation for the background field numerically.

A.2 Solving the differential equations

We write the original second order differential equation as two coupled first-order equations; in matrix form:

$$\partial_t x(t) = U(t)x(t), \quad (\text{A.3})$$

with

$$x = \begin{pmatrix} \delta\phi_k \\ \delta\pi_k \end{pmatrix}; \quad U(t) = \begin{pmatrix} 0 & 1 \\ -k^2 - V''(\phi) & 0 \end{pmatrix}. \quad (\text{A.4})$$

The variable $\delta\pi_k = \delta\dot{\phi}_k$ is introduced for convenience.

Introduce the fundamental matrix such that¹³

$$x(t) = \mathcal{O}(t, t_0)x(t_0) \quad (\text{A.5})$$

with boundary condition

$$\mathcal{O}(t_0, t_0) = \mathbb{1}. \quad (\text{A.6})$$

From eq.(A.3) we have

$$\partial_t \mathcal{O}(t, t_0) = U(t)\mathcal{O}(t, t_0). \quad (\text{A.7})$$

The Floquet theorem states that the fundamental matrix can be expressed as

$$\mathcal{O}(t, t_0) = P(t, t_0) \exp[(t - t_0)\Lambda(t_0)] \quad (\text{A.8})$$

where $\Lambda(t_0)$ is defined via $\mathcal{O}(t_0 + T, t_0) = \exp[T\Lambda(t_0)]$, and P is periodic, i.e. $P(t + T, t_0) = P(t, t_0)$. Both $P(t, t_0)$ and $\Lambda(t_0)$ are matrices. The eigenvalues of $\Lambda(t_0)$ are the Floquet exponents. $x(t)$ can then be expressed in terms of the eigenbasis of $\Lambda(t_0)$:

$$\begin{aligned} x(t) &= \mathcal{O}(t, t_0)x(t_0), \\ &= \sum_{s=1}^2 P(t, t_0)c_s \exp[(t - t_0)\Lambda(t_0)]e_s(t_0), \\ &= \sum_{s=1}^2 c_s P(t, t_0)e_s(t_0)e^{\mu_k^s(t-t_0)}, \end{aligned}$$

with $x(t_0) = \sum_{s=1}^2 c_s e_s(t_0)$ and $\Lambda(t_0)e_s(t_0) = \mu_k^s(t_0)e_s(t_0)$ ¹⁴.

After diagonalizing the fundamental matrix $\mathcal{O}(t_0 + T, t_0)$, the real part of the Floquet exponents are

$$\Re(\mu_k^s) = \frac{1}{T} \ln |o_k^s|, \quad (\text{A.9})$$

with o_k^s the eigenvalues of $\mathcal{O}(t_0 + T, t_0)$.

A.3 Abel's identity

As a consequence of Abel's identity, the sum of Floquet exponents must be zero [74]

$$\sum_{s=1}^2 \mu_k^s = \frac{1}{T} \ln \left(\prod_{s=1}^2 o_k^s \right) = \frac{1}{T} \ln \det \mathcal{O}. \quad (\text{A.10})$$

¹³Note that off-diagonal elements of \mathcal{O} can have non-zero mass dimensions!

¹⁴One can see this from $Q^{-1}AQ = A_{\text{diag}} \Rightarrow AQ = QA_{\text{diag}}$ and Q 's columns are the eigenvectors.

Since the trace of U in (A.4) vanishes, the Wronski determinant computed from the n eigenvalues of \mathcal{O} must be conserved by Abel's identity [75]:

$$W(t) = W(t_0) \exp\left(\int_{t_0}^t dt' \operatorname{tr}(U(t'))\right), \quad (\text{A.11})$$

where we have used eq.(A.7). From the initial conditions (A.6), we then have

$$\sum_{s=1}^2 \mu_k^s = \frac{1}{T} \ln \det \mathbb{1} = 0. \quad (\text{A.12})$$

This can be used as a consistency check after computing each individual Floquet exponent. The differential equations seem really stiff; thus we choose to use the implicit Runge–Kutta method of order 5 implemented in [20, 21] for the numerical solution.

B Lattice parameters

ϕ_0/m_{Pl}	0.1	0.01	$5 \cdot 10^{-3}$	10^{-3}	10^{-4}
N	256	256	256	256	256
tMax	200	200	300	500	500
dt	0.005	0.005	0.005	0.005	0.005
kIR	0.25	0.25	0.25	0.25	0.25
kCutoff	55	55	55	55	55
init. amp./GeV	1.15×10^{17}	1.16×10^{16}	5.74×10^{15}	1.15×10^{15}	1.11×10^{14}
init. mom./GeV ²	-7.07×10^{25}	-7.41×10^{22}	-9.27×10^{21}	-7.42×10^{19}	-7.67×10^{16}

Table 2: Lattice parameters for various ϕ_0 's. Except for the initial amplitudes (**init. amp.**) and initial momenta (**init. mom.**), all quantities are given in program units.

C Virial theorem

Heuristically, one can derive the Virial theorem from the (full) equation of motion

$$\ddot{\phi} - \frac{1}{a^2} \nabla^2 \phi + 3H\dot{\phi} + \frac{\partial V}{\partial \phi} = 0. \quad (\text{C.1})$$

Ignore the Hubble term for now. One can multiply all remaining terms with ϕ and take the volume average:

$$\left\langle \phi \ddot{\phi} \right\rangle - \frac{1}{a^2} \left\langle \phi \nabla^2 \phi \right\rangle + \left\langle \phi \frac{\partial V}{\partial \phi} \right\rangle = 0. \quad (\text{C.2})$$

Assuming the surface terms will fall off fast enough, one obtains the virial theorem after integration by parts and averaging over time:

$$\frac{1}{2} \left\langle \dot{\phi}^2 \right\rangle - \frac{1}{2a^2} \left\langle (\nabla \phi)^2 \right\rangle - \frac{1}{2} \left\langle \phi \frac{\partial V}{\partial \phi} \right\rangle = 0, \quad (\text{C.3})$$

where the three terms can be interpreted as kinetic, gradient and potential energy, respectively.

This heuristic derivation neglects the Hubble friction term and the surface terms in the integration by parts. More rigorously, one can show the same relation by using the general virial theorem in statistical physics

$$\left\langle \eta_i(x) \frac{\partial \mathcal{H}}{\partial \eta_j(y)} \right\rangle = T \delta_{ij} \delta(x - y), \quad (\text{C.4})$$

with $\eta_i = \phi, \dot{\phi}$ [76, 77].

D Propagation of gravitational waves

In order to obtain the current frequency and scaled energy density of GWs, one has to compute the redshifting due to the expansion of the universe between the time of GW production and today. Note that entropy is not conserved until thermalization by inflaton decay has completed. We therefore factorize the relevant ratio of scale factors, for later convenience we also introduce additional factors involving densities that multiply to unity:

$$\frac{a_p}{a_0} = \frac{a_p}{a_{\text{th}}} \cdot \frac{a_{\text{th}}}{a_0} \cdot \frac{1}{\rho_{c,p}^{1/4}} \left(\frac{\rho_{c,p}}{\rho_{c,\text{th}}} \right)^{1/4} \rho_{c,\text{th}}^{1/4}. \quad (\text{D.1})$$

Here $\rho_{c,p}$ and $\rho_{c,\text{th}}$ refer to the critical energy density of the Universe at time of GW production and thermalization, respectively; since to excellent approximation $\Omega_{\text{tot}} = 1$ after inflation, the critical energy density can be equated with the total energy density.

For a general time-dependent equation of state parameter $\omega(t)$, one has

$$\frac{\rho_p}{\rho_{\text{th}}} = \exp \left[-3 \int_{a_{\text{th}}}^{a_p} (1 + \omega) d(\ln \tilde{a}) \right] = \left(\frac{a_p}{a_{\text{th}}} \right)^{-3(1+\omega)}. \quad (\text{D.2})$$

In the second step we have made the simplifying assumption that ω is constant till thermalization. This yields

$$\frac{a_p}{a_{\text{th}}} \left(\frac{\rho_{c,p}}{\rho_{c,\text{th}}} \right)^{1/4} = \left(\frac{a_p}{a_{\text{th}}} \right)^{(1-3\omega)/4} \lesssim 1. \quad (\text{D.3})$$

Standard thermalization takes the Universe from matter domination (coherent, harmonic oscillation of the inflaton field) to radiation domination (the hot Big Bang), in which case the average value of ω should be somewhere in between 0 and 1/3. In our case the initial oscillations are quite anharmonic, leading to $\omega < 0$ initially, see fig. 9; later ω is positive but quite small. For the sake of giving a definitive estimate of the current peak frequency of GW, we take this factor to be unity.

If the entropy is conserved, then

$$S \propto g_{*,s}(T) T^3 a^3 = \text{const}. \quad (\text{D.4})$$

As long as $g_{*,s} \simeq g_*$ the (relativistic) energy density¹⁵ scales like

$$\rho \propto g_* T^4 \propto g_*^{-1/3} a^{-4}. \quad (\text{D.5})$$

Since at reheating, $\rho_{\text{rel,th}} \simeq \rho_{\text{tot,th}} = \rho_{c,\text{th}}$, we have

$$\frac{a_{\text{th}}}{a_0} = \left(\frac{\rho_{\text{rel,0}}}{\rho_{c,\text{th}}} \right)^{1/4} \left(\frac{g_{*,0}}{g_{*,\text{th}}} \right)^{1/12}. \quad (\text{D.6})$$

¹⁵Only radiation contributes to entropy at leading order.

Inserting eqs.(D.3) and (D.6) back into (D.1), one has

$$\frac{a_p}{a_0} \simeq \left(\frac{\rho_{\text{rel},0}}{\rho_{c,p}} \right)^{1/4} \left(\frac{g_{*,0}}{g_{*,\text{th}}} \right)^{1/12}. \quad (\text{D.7})$$

The last factor depends on the reheat temperature only very weakly, due to the power $1/12$. Even if all Standard Model degrees of freedom contribute at T_{th} , $g_{*,0}/g_{*,\text{th}} \approx 0.032$ in which case the last factor in eq.(D.7) is about 0.75; for T_{th} below the mass of the top quark this factor would be even closer to 1.

Today's radiation energy density can be computed from the CMB monopole temperature

$$\rho_{\text{rel},0} = 2 \frac{\pi^2}{30} T_0^4 = 1.93 \times 10^{-15} \text{ eV}^4. \quad (\text{D.8})$$

Hence,

$$\frac{a_p}{a_0} \simeq 1.57 \times 10^{-13} \frac{\text{GeV}}{\rho_{c,p}^{1/4}}. \quad (\text{D.9})$$

The possibility to detect GWs crucially depends on their frequency today. For a metric perturbation of fixed comoving size k_{gw} today's frequency is [10]

$$f_0 = \frac{1}{2\pi} \frac{k_{\text{gw}}}{a_p} \frac{a_p}{a_0} \simeq \frac{k_{\text{gw}}}{a_p} \frac{1}{\rho_{c,p}^{1/4}} \cdot 3.80 \times 10^{10} \text{ Hz}. \quad (\text{D.10})$$

The first factor is just the physical wavelength of the GW at time of production. The physical interpretation of the $\rho_{c,p}^{-1/4}$ factor is clear: the higher the energy scale at production, the more expansion the mode would experience in the past, leading to a longer wavelength and lower frequency. Note that $\rho_{c,p}$ in the numerical result is taken at the same time as the GW spectrum.

Of course, only sufficiently strong GW signals are detectable. GWs are radiation, thus their energy density decays like a^{-4} . At a general temperature after production, the scaled energy density becomes

$$\begin{aligned} \Omega_{\text{gw}}(T) h^2 &= \Omega_{\text{gw},p} h^2 \frac{\rho_{c,p}}{\rho_c(T)} \left(\frac{a_p}{a(T)} \right)^4, \\ &= \Omega_{\text{gw},p} h^2 \frac{\rho_{\text{rel}}(T)}{\rho_c(T)} \left(\frac{g_*(T)}{g_{*,\text{SM}}} \right)^{1/3}, \end{aligned} \quad (\text{D.11})$$

where eq.(D.6) has been used in the second step. Under the above assumptions, this yields for the current Universe

$$\Omega_{\text{gw},0} h^2 = 7.81 \times 10^{-6} \cdot \Omega_{\text{gw},p} h^2. \quad (\text{D.12})$$

E Dependence on the reheating temperature

So far we have assumed that the factor appearing in eq.(D.3) can be set to unity. This allowed us to derive expressions for today's peak frequency and energy density of GWs that are independent of the reheat temperature. In this Appendix we estimate this factor slightly more carefully.

For a general ω parameter, we have

$$\frac{a(t)}{a_i} = \left[\frac{3(\omega+1)}{2} H_i(t-t_i) + 1 \right]^{\frac{2}{3(\omega+1)}}, \quad (\text{E.1})$$

where t_i , a_i and H_i are the initial cosmic time, the initial scale factor and Hubble parameter, respectively. As a generous estimate, we take $H_{\text{gw}} \simeq H_I$ and $t_{\text{reheating}} = 1/\Gamma_\phi = 8\pi/y^2 m_\phi$, where we have computed the inflaton decay width Γ_ϕ under the assumption that it decays into a fermion pair via a Yukawa coupling y [8]. Thermalization is assumed to be completed instantaneously after perturbative reheating. Then we define

$$A := \left(\frac{a_p}{a_{\text{th}}}\right)^{(1-3\omega)/4} \simeq \left[\frac{3(\omega+1)}{2} \frac{\sqrt{d}\phi_0^2}{3m_{\text{Pl}} y^2 \cdot 2\sqrt{d}\phi_0}\right]^{\frac{-1+3\omega}{6(1+\omega)}} = \left[2\pi(1+\omega) \frac{\phi_0}{m_{\text{Pl}}} \frac{1}{y^2}\right]^{\frac{-1+3\omega}{6(1+\omega)}}. \quad (\text{E.2})$$

Evidently, if we had radiation domination, $\omega = 1/3$, during perturbative reheating, this factor would be unity, since then ρ_{gw} would redshift exactly like ρ_{tot} . For matter domination, $\omega = 0$, the exponent is $-1/6$. Putting in this number, the left frame of fig. 21 shows that A can be up to five orders of magnitudes lower than unity. Thus, the GW frequency will get shifted to smaller values, where planned experiments are more sensitive; however, Ω_{gw} will be reduced as well. As indicated in eq.(E.2), A becomes larger with decreasing ϕ_0 , which decreases the expansion rate during this epoch, but decreases with decreasing y , which delays the completion of reheating.

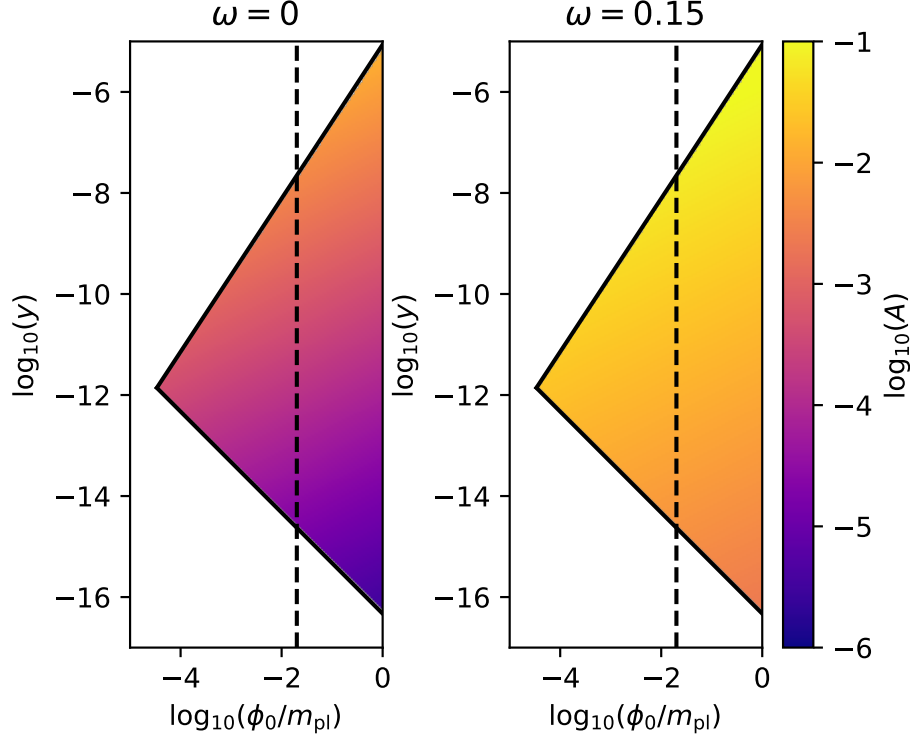


Figure 21: Results for the factor A defined in eq.(E.2) for constant $\omega = 0$ (left) and $\omega = 0.15$ (right) from the time of GW production until the end of reheating. The latter proceeds through perturbative inflaton decay via a Yukawa coupling y . The upper and lower bounds on y come from the radiative stability of the inflaton potential and successful Big Bang nucleosynthesis, respectively [8]. The color corresponds to the logarithm of A . GW production from the formation of oscillons is significant only to the left of the dashed lines..

Recall that ω is slightly positive while the oscillons exist, see fig. 9; moreover, more realistically a significant radiation component will build up before reheating is completed. Both effects will tend to increase ω , and thus A . An example is shown in the right frame of fig. 21, where we have set

$\omega = 0.15$. This changes the power in eq.(E.2) to about -0.08 , leading to a much weaker dependence on ϕ_0 and y than in the case with $\omega = 0$. Now A is typically $\mathcal{O}(0.1)$ or slightly smaller.

The exact value of ω is thus quite important here. As already noted, during oscillon formation ω is positive but small. Oscillons will eventually decay. According to [18, 46, 50, 78], this happens via the emission of inflaton particles with typical momentum $p \sim m_\phi$; this should lead to an at least temporary increase of ω . Finally, as already noted, a precise computation of A would have to include the increase of ω due to the gradual build-up of the radiation component.

References

- [1] D. Baumann. In *Theoretical Advanced Study Institute in Elementary Particle Physics: Physics of the Large and the Small*. 2011 pp. 523. DOI: [10.1142/9789814327183_0010](#). arXiv: [0907.5424 \[hep-th\]](#).
- [2] S. Dodelson. AIP Conf. Proc. 689.1 (2003). Ed. by J. F. Nieves and R. R. Volkas 184. DOI: [10.1063/1.1627736](#). arXiv: [hep-ph/0309057](#).
- [3] N. Aghanim et al. Astron. Astrophys. 641 (2020). [Erratum: Astron.Astrophys. 652, C4 (2021)] A6. DOI: [10.1051/0004-6361/201833910](#). arXiv: [1807.06209 \[astro-ph.CO\]](#).
- [4] L. Kofman, A. D. Linde, and A. A. Starobinsky. Phys. Rev. D 56 (1997) 3258–3295. DOI: [10.1103/PhysRevD.56.3258](#). arXiv: [hep-ph/9704452](#).
- [5] D. J. H. Chung, E. W. Kolb, A. Riotto, and I. I. Tkachev. Phys. Rev. D 62 (2000) 043508. DOI: [10.1103/PhysRevD.62.043508](#). arXiv: [hep-ph/9910437](#).
- [6] E. J. Copeland, S. Pascoli, and A. Rajantie. Phys. Rev. D 65 (2002) 103517. DOI: [10.1103/PhysRevD.65.103517](#). arXiv: [hep-ph/0202031](#).
- [7] J. F. Dufaux et al. JCAP 07 (2006) 006. DOI: [10.1088/1475-7516/2006/07/006](#). arXiv: [hep-ph/0602144](#).
- [8] M. Drees and Y. Xu. JCAP 09 (2021) 012. DOI: [10.1088/1475-7516/2021/09/012](#). arXiv: [2104.03977 \[hep-ph\]](#).
- [9] M. A. Amin and D. Shirokoff. Phys. Rev. D 81 (2010) 085045. DOI: [10.1103/PhysRevD.81.085045](#). arXiv: [1002.3380 \[astro-ph.CO\]](#).
- [10] K. D. Lozanov and M. A. Amin. Phys. Rev. D 99.12 (2019) 123504. DOI: [10.1103/PhysRevD.99.123504](#). arXiv: [1902.06736 \[astro-ph.CO\]](#).
- [11] X.-X. Kou, C. Tian, and S.-Y. Zhou. Class. Quant. Grav. 38.4 (2021) 045005. DOI: [10.1088/1361-6382/abd09f](#). arXiv: [1912.09658 \[gr-qc\]](#).
- [12] Z. Nazari, M. Cicoli, K. Clough, and F. Muia. JCAP 05 (2021) 027. DOI: [10.1088/1475-7516/2021/05/027](#). arXiv: [2010.05933 \[gr-qc\]](#).
- [13] Z. Huang. Phys. Rev. D 83 (2011) 123509. DOI: [10.1103/PhysRevD.83.123509](#). arXiv: [1102.0227 \[astro-ph.CO\]](#).
- [14] S.-Y. Zhou et al. JHEP 10 (2013) 026. DOI: [10.1007/JHEP10\(2013\)026](#). arXiv: [1304.6094 \[astro-ph.CO\]](#).
- [15] S. Antusch, F. Cefala, and S. Orani. Phys. Rev. Lett. 118.1 (2017). [Erratum: Phys.Rev.Lett. 120, 219901 (2018)] 011303. DOI: [10.1103/PhysRevLett.118.011303](#). arXiv: [1607.01314 \[astro-ph.CO\]](#).

- [16] S. Antusch, F. Cefala, and S. Orani. JCAP 03 (2018) 032. DOI: [10.1088/1475-7516/2018/03/032](https://doi.org/10.1088/1475-7516/2018/03/032). arXiv: [1712.03231](https://arxiv.org/abs/1712.03231) [[astro-ph.CO](#)].
- [17] M. A. Amin et al. Phys. Rev. D 98 (2018) 024040. DOI: [10.1103/PhysRevD.98.024040](https://doi.org/10.1103/PhysRevD.98.024040). arXiv: [1803.08047](https://arxiv.org/abs/1803.08047) [[astro-ph.CO](#)].
- [18] K. D. Lozanov and V. Takhistov. Phys. Rev. Lett. 130.18 (2023) 181002. DOI: [10.1103/PhysRevLett.130.181002](https://doi.org/10.1103/PhysRevLett.130.181002). arXiv: [2204.07152](https://arxiv.org/abs/2204.07152) [[astro-ph.CO](#)].
- [19] M. A. Amin, M. P. Hertzberg, D. I. Kaiser, and J. Karouby. Int. J. Mod. Phys. D 24 (2014) 1530003. DOI: [10.1142/S0218271815300037](https://doi.org/10.1142/S0218271815300037). arXiv: [1410.3808](https://arxiv.org/abs/1410.3808) [[hep-ph](#)].
- [20] P. Virtanen et al. Nature Meth. 17 (2020) 261. DOI: [10.1038/s41592-019-0686-2](https://doi.org/10.1038/s41592-019-0686-2). arXiv: [1907.10121](https://arxiv.org/abs/1907.10121) [[cs.MS](#)].
- [21] C. R. Harris et al. Nature 585.7825 (2020) 357–362. DOI: [10.1038/s41586-020-2649-2](https://doi.org/10.1038/s41586-020-2649-2). arXiv: [2006.10256](https://arxiv.org/abs/2006.10256) [[cs.MS](#)].
- [22] F. Pedregosa et al. J. Machine Learning Res. 12 (2011) 2825. arXiv: [1201.0490](https://arxiv.org/abs/1201.0490) [[cs.LG](#)].
- [23] J. D. Hunter. Comput. Sci. Eng. 9.3 (2007) 90. DOI: [10.1109/MCSE.2007.55](https://doi.org/10.1109/MCSE.2007.55).
- [24] C. Bane Sullivan and A. Kaszynski. Journal of Open Source Software 4.37 (2019) 1450. DOI: [10.21105/joss.01450](https://doi.org/10.21105/joss.01450).
- [25] A. Collette. *Python and HDF5*. O'Reilly, 2013.
- [26] D. G. Figueroa, A. Florio, F. Torrenti, and W. Valkenburg. Comput. Phys. Commun. 283 (2023) 108586. DOI: [10.1016/j.cpc.2022.108586](https://doi.org/10.1016/j.cpc.2022.108586). arXiv: [2102.01031](https://arxiv.org/abs/2102.01031) [[astro-ph.CO](#)].
- [27] M. Drees and Y. Xu. JCAP 12 (2022) 005. DOI: [10.1088/1475-7516/2022/12/005](https://doi.org/10.1088/1475-7516/2022/12/005). arXiv: [2209.07545](https://arxiv.org/abs/2209.07545) [[astro-ph.CO](#)].
- [28] Y. Akrami et al. Astron. Astrophys. 641 (2020) A10. DOI: [10.1051/0004-6361/201833887](https://doi.org/10.1051/0004-6361/201833887). arXiv: [1807.06211](https://arxiv.org/abs/1807.06211) [[astro-ph.CO](#)].
- [29] D. H. Lyth and A. R. Liddle. *The primordial density perturbation: Cosmology, inflation and the origin of structure*. 2009.
- [30] J. J. Sakurai and J. Napolitano. *Modern Quantum Mechanics*. Quantum physics, quantum information and quantum computation. Cambridge University Press, Oct. 2020. ISBN: 978-0-8053-8291-4, 978-1-108-52742-2, 978-1-108-58728-0. DOI: [10.1017/9781108587280](https://doi.org/10.1017/9781108587280).
- [31] J. Mathews and R. Walker. *Mathematical Methods of Physics*. California Institute of Technology, 1970.
- [32] M. A. Amin, M. P. Hertzberg, D. I. Kaiser, and J. Karouby. International Journal of Modern Physics D 24.01 (Jan. 2015) 1530003. ISSN: 0218-2718, 1793-6594. DOI: [10.1142/S0218271815300037](https://doi.org/10.1142/S0218271815300037). arXiv: [1410.3808](https://arxiv.org/abs/1410.3808).
- [33] A. Karam, E. Tomberg, and H. Veermäe. JCAP 06 (2021) 023. DOI: [10.1088/1475-7516/2021/06/023](https://doi.org/10.1088/1475-7516/2021/06/023). arXiv: [2102.02712](https://arxiv.org/abs/2102.02712) [[astro-ph.CO](#)].
- [34] D. Polarski and A. A. Starobinsky. Class. Quant. Grav. 13 (1996) 377–392. DOI: [10.1088/0264-9381/13/3/006](https://doi.org/10.1088/0264-9381/13/3/006). arXiv: [gr-qc/9504030](https://arxiv.org/abs/gr-qc/9504030).
- [35] S. Y. Khlebnikov and I. I. Tkachev. Phys. Rev. Lett. 77 (1996) 219–222. DOI: [10.1103/PhysRevLett.77.219](https://doi.org/10.1103/PhysRevLett.77.219). arXiv: [hep-ph/9603378](https://arxiv.org/abs/hep-ph/9603378).
- [36] M. A. Amin. (Sept. 2010). arXiv: [1006.3075](https://arxiv.org/abs/1006.3075).

- [37] N. Koivunen, E. Tomberg, and H. Veermäe. JCAP 07.07 (2022) 028. DOI: [10.1088/1475-7516/2022/07/028](#). arXiv: [2201.04145 \[astro-ph.CO\]](#).
- [38] M. Desroche, G. N. Felder, J. M. Kratochvil, and A. Linde. Physical Review D 71.10 (May 20, 2005) 103516. ISSN: 1550-7998, 1550-2368. DOI: [10.1103/PhysRevD.71.103516](#). arXiv: [hep-th/0501080](#). URL: <http://arxiv.org/abs/hep-th/0501080> (visited on 09/09/2021).
- [39] K. Kainulainen, S. Nurmi, and O. Väisänen. *Tachyonic production of dark relics: classical lattice vs. quantum 2PI in Hartree truncation*. 2024. arXiv: [2406.17468 \[hep-ph\]](#). URL: <https://arxiv.org/abs/2406.17468>.
- [40] G. N. Felder and L. Kofman. Phys. Rev. D 75 (2007) 043518. DOI: [10.1103/PhysRevD.75.043518](#). arXiv: [hep-ph/0606256](#).
- [41] I. L. Bogolyubsky and V. G. Makhankov. JETP Lett. 24 (1976) 12.
- [42] M. Gleiser. Phys. Rev. D 49 (1994) 2978–2981. DOI: [10.1103/PhysRevD.49.2978](#). arXiv: [hep-ph/9308279](#).
- [43] E. J. Copeland, M. Gleiser, and H.-R. Muller. Phys. Rev. D 52 (1995) 1920–1933. DOI: [10.1103/PhysRevD.52.1920](#). arXiv: [hep-ph/9503217](#).
- [44] G. H. Derrick. J. Math. Phys. 5 (1964) 1252–1254. DOI: [10.1063/1.1704233](#).
- [45] R. Mahbub and S. S. Mishra. Physical Review D 108.6 (Sept. 27, 2023) 063524. ISSN: 2470-0010, 2470-0029. DOI: [10.1103/PhysRevD.108.063524](#). arXiv: [2303.07503 \[astro-ph, physics:gr-qc\]](#). URL: <http://arxiv.org/abs/2303.07503> (visited on 07/10/2024).
- [46] H.-Y. Zhang et al. JCAP 07 (2020) 055. DOI: [10.1088/1475-7516/2020/07/055](#). arXiv: [2004.01202 \[hep-th\]](#).
- [47] K. Mukaida, M. Takimoto, and M. Yamada. JHEP 03 (2017) 122. DOI: [10.1007/JHEP03\(2017\)122](#). arXiv: [1612.07750 \[hep-ph\]](#).
- [48] D. G. Levkov, V. E. Maslov, E. Y. Nugaev, and A. G. Panin. JHEP 12 (2022) 079. DOI: [10.1007/JHEP12\(2022\)079](#). arXiv: [2208.04334 \[hep-th\]](#).
- [49] S. Antusch, F. Cefalà, and F. Torrentí. JCAP 10 (2019) 002. DOI: [10.1088/1475-7516/2019/10/002](#). arXiv: [1907.00611 \[hep-ph\]](#).
- [50] P. Salmi and M. Hindmarsh. Phys. Rev. D 85 (2012) 085033. DOI: [10.1103/PhysRevD.85.085033](#). arXiv: [1201.1934 \[hep-th\]](#).
- [51] Dmitry S Gorbunov and Valery A Rubakov. *Introduction to the Theory of the Early Universe: Cosmological Perturbations and Inflationary Theory*. World Scientific Publishing Co. Pte. Ltd., 2011. ISBN: 978-981-4322-22-5.
- [52] Steven Weinberg. *Gravitation and Cosmology: Principles and Applications of the General Theory of Relativity*. John Wiley & Sons, 1972. ISBN: 0-471-92567-5.
- [53] B. J. Carr, K. Kohri, Y. Sendouda, and J. Yokoyama. Phys. Rev. D 94.4 (2016) 044029. DOI: [10.1103/PhysRevD.94.044029](#). arXiv: [1604.05349 \[astro-ph.CO\]](#).
- [54] D. H. Lyth, K. A. Malik, M. Sasaki, and I. Zaballa. JCAP 01 (2006) 011. DOI: [10.1088/1475-7516/2006/01/011](#). arXiv: [astro-ph/0510647](#).
- [55] S. Young and C. T. Byrnes. JCAP 08 (2013) 052. DOI: [10.1088/1475-7516/2013/08/052](#). arXiv: [1307.4995 \[astro-ph.CO\]](#).

- [56] T. Suyama, T. Tanaka, B. Bassett, and H. Kudoh. JCAP 04 (2006) 001. DOI: [10.1088/1475-7516/2006/04/001](#). arXiv: [hep-ph/0601108](#).
- [57] E. Cotner, A. Kusenko, M. Sasaki, and V. Takhistov. JCAP 10 (2019) 077. DOI: [10.1088/1475-7516/2019/10/077](#). arXiv: [1907.10613 \[astro-ph.CO\]](#).
- [58] E. Cotner, A. Kusenko, and V. Takhistov. Phys. Rev. D 98.8 (2018) 083513. DOI: [10.1103/PhysRevD.98.083513](#). arXiv: [1801.03321 \[astro-ph.CO\]](#).
- [59] E. Torres-Lomas, J. C. Hidalgo, K. A. Malik, and L. A. Ureña-López. Phys. Rev. D 89.8 (2014) 083008. DOI: [10.1103/PhysRevD.89.083008](#). arXiv: [1401.6960 \[astro-ph.CO\]](#).
- [60] J. C. Aurrekoetxea, K. Clough, and F. Muia. Phys. Rev. D 108.2 (2023) 023501. DOI: [10.1103/PhysRevD.108.023501](#). arXiv: [2304.01673 \[gr-qc\]](#).
- [61] C. Caprini and D. G. Figueroa. Class. Quant. Grav. 35.16 (2018) 163001. DOI: [10.1088/1361-6382/aac608](#). arXiv: [1801.04268 \[astro-ph.CO\]](#).
- [62] X.-X. Kou, J. B. Mertens, C. Tian, and S.-Y. Zhou. Phys. Rev. D 105.12 (2022) 123505. DOI: [10.1103/PhysRevD.105.123505](#). arXiv: [2112.07626 \[gr-qc\]](#).
- [63] George David Birkhoff and Rudolph Ernest Langer. *Relativity and Modern Physics*. Harvard University Press, 1927. ISBN: 978-0-674-73024-3.
- [64] J. F. Dufaux et al. Phys. Rev. D 76 (2007) 123517. DOI: [10.1103/PhysRevD.76.123517](#). arXiv: [0707.0875 \[astro-ph\]](#).
- [65] D. G. Figueroa, A. Florio, F. Torrenti, and W. Valkenburg. JCAP 04 (2021) 035. DOI: [10.1088/1475-7516/2021/04/035](#). arXiv: [2006.15122 \[astro-ph.CO\]](#).
- [66] J. Baeza-Ballesteros, A. Florio, and N. Loayza. () 14. URL: https://cosmolattice.net/assets/technical_notes/CosmoLattice_TechnicalNote_GWs.pdf.
- [67] K. Schmitz. JHEP 01 (2021) 097. DOI: [10.1007/JHEP01\(2021\)097](#). arXiv: [2002.04615 \[hep-ph\]](#).
- [68] N. Aggarwal et al. Living Rev. Rel. 24.1 (2021) 4. DOI: [10.1007/s41114-021-00032-5](#). arXiv: [2011.12414 \[gr-qc\]](#).
- [69] R. H. Cyburt, B. D. Fields, K. A. Olive, and E. Skillman. Astropart. Phys. 23 (2005) 313–323. DOI: [10.1016/j.astropartphys.2005.01.005](#). arXiv: [astro-ph/0408033](#).
- [70] K. D. Lozanov and M. A. Amin. Phys. Rev. D 97.2 (2018) 023533. DOI: [10.1103/PhysRevD.97.023533](#). arXiv: [1710.06851 \[astro-ph.CO\]](#).
- [71] K. D. Lozanov and M. A. Amin. Phys. Rev. D 90.8 (2014) 083528. DOI: [10.1103/PhysRevD.90.083528](#). arXiv: [1408.1811 \[hep-ph\]](#).
- [72] M. A. Amin and P. Mocz. Phys. Rev. D 100.6 (2019) 063507. DOI: [10.1103/PhysRevD.100.063507](#). arXiv: [1902.07261 \[astro-ph.CO\]](#).
- [73] F. M. Hahne, P. Klimas, J. S. Streibel, and W. J. Zakrzewski. JHEP 01 (2020) 006. DOI: [10.1007/JHEP01\(2020\)006](#). arXiv: [1909.01992 \[hep-th\]](#).
- [74] M. A. Amin, P. Zukin, and E. Bertschinger. Phys. Rev. D 85 (2012) 103510. DOI: [10.1103/PhysRevD.85.103510](#). arXiv: [1108.1793 \[astro-ph.CO\]](#).
- [75] Teschl, Gerald. *Ordinary Differential Equations and Dynamical Systems*. Providence: American Mathematical Society, 2020. ISBN: 978-0-8218-8328-0.
- [76] P. F. Schwabl. *Statistical Mechanics*. Springer, 2006. ISBN: 978-3-540-32343-3.

- [77] D. Boyanovsky, C. Destri, and H. J. de Vega. Phys. Rev. D 69 (2004) 045003. DOI: [10.1103/PhysRevD.69.045003](#). arXiv: [hep-ph/0306124](#).
- [78] M. P. Hertzberg. Phys. Rev. D 82 (2010) 045022. DOI: [10.1103/PhysRevD.82.045022](#). arXiv: [1003.3459 \[hep-th\]](#).